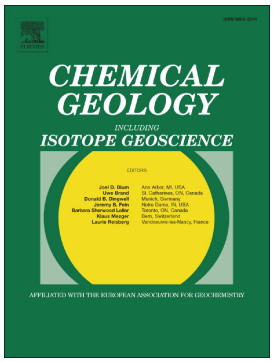

Alkali-carbonate melts from the base of cratonic lithospheric mantle: Links to kimberlites

Alexander V. Golovin, Igor S. Sharygin, Vadim S. Kamenetsky, Andrey V. Korsakov, Gregory M. Yaxley

PII: S0009-2541(18)30081-0
DOI: doi:10.1016/j.chemgeo.2018.02.016
Reference: CHEMGE 18655

To appear in: *Chemical Geology*

Received date: 29 April 2017
Revised date: 7 February 2018
Accepted date: 8 February 2018

Please cite this article as: Alexander V. Golovin, Igor S. Sharygin, Vadim S. Kamenetsky, Andrey V. Korsakov, Gregory M. Yaxley , Alkali-carbonate melts from the base of cratonic lithospheric mantle: Links to kimberlites. The address for the corresponding author was captured as affiliation for all authors. Please check if appropriate. Chemge(2018), doi:10.1016/j.chemgeo.2018.02.016

Alkali-carbonate melts from the base of cratonic lithospheric mantle: links to kimberlites

Alexander V. Golovin[1,2]*, Igor S. Sharygin[1], Vadim S. Kamenetsky[3], Andrey V. Korsakov[1], Gregory M. Yaxley[4]

[1] *Sobolev Institute of Geology and Mineralogy, Siberian Branch Russian Academy of Sciences, Koptyuga Pr. 3, Novosibirsk 630090, Russian Federation*

[2] *Diamond and Precious Metal Geology Institute, Siberian Branch Russian Academy of Sciences, Lenina Pr. 39, Yakutsk 677000, Russian Federation*

[3] *School of Physical Sciences, University of Tasmania, Hobart, Tasmania 7001, Australia*

[4] *Research School of Earth Sciences, The Australian National University, Canberra ACT 2601, Australia*

*Corresponding author: Alexander V. Golovin, e-mail: *avg@igm.nsc.ru*

Highlights:

We studied melt inclusions in olivine of sheared peridotite xenoliths from kimberlites

These xenoliths are derived from 180–230 km and are among the deepest mantle rocks

Alkali-rich carbonates, halides, sulphates and aragonite were found in melt inclusions

Melt inclusions are snapshots Cl–S–alkali-rich carbonate melt originated at > 230 km

The high-pressure melt inclusions may represent near primary kimberlite melt

Abstract

Identification of the primary compositions of mantle-derived melts is crucial for understanding mantle compositions and physical conditions of mantle melting. However, these melts rarely reach the Earth's surface unmodified because of contamination, crystal fractionation and degassing, processes that occur almost ubiquitously after melt generation. Here we report snapshots of the melts preserved in sheared peridotite xenoliths from the

Udachnaya-East kimberlite pipe, in the central part of the Siberian craton. These xenoliths are among the deepest mantle samples and were delivered by kimberlite magma from 180–230 km depth, i.e. from the base of the cratonic lithosphere. The olivine grains of the sheared peridotites contain secondary inclusions of the crystallized melt with bulk molar (Na + K)/Ca ~ 3.4. Various Na-K-Ca-, Na-Ca-, Na-Mg-, Ca-Mg- and Ca-carbonates, Na-Mg-carbonates with additional anions, alkali sulphates and halides are predominant among the daughter minerals in secondary melt inclusions, whereas silicates, oxides, sulphides and phosphates are subordinate. These inclusions can be considered as Cl–S-bearing alkali-carbonate melts. The presence of aragonite, a high-pressure polymorph of $CaCO_3$, among the daughter minerals suggests a mantle origin for these melt inclusions. The secondary melt inclusions in olivine from the sheared peridotite xenoliths and the melt inclusions in phenocrystic olivines from the host kimberlites demonstrate similarities, in daughter minerals assemblages and trace-element compositions. Moreover, alkali-rich minerals (carbonates, halides, sulphates and sulphides) identified in the studied melt inclusions are also present in the groundmass of the host kimberlites. These data suggests a genetic link between melt enclosed in olivine from the sheared peridotites and melt parental to the Udachnaya-East kimberlites. We suggest that the melt inclusions in olivine from mantle xenoliths may represent near primary, kimberlite melts. These results are new evidence in support of the alkali-carbonate composition of kimberlite melts in their source regions, prior to the kimberlite emplacement into the crust, and are in stark contrast to the generally accepted ultramafic silicate nature of parental kimberlite liquids.

1. Introduction

It is widely accepted that mantle-derived carbonatite and carbonate-rich melts play an important role in metasomatic modifications of mantle compositions and mineral-forming reactions involving the formation of diamonds. The stability of carbonate minerals and

carbonate-rich melts in the mantle is supported by numerous high-pressure experimental studies of both carbonated peridotite and eclogite lithologies (e.g. Wallace and Green, 1988; Dalton and Wood, 1993; Dasgupta et al., 2013; Litasov et al., 2013). Such melts inevitably interact with mantle rocks and modify their modal mineralogy and major and the trace element budgets of individual minerals. The geochemical effects of carbonatitic metasomatism in the mantle have been recognized in mantle xenoliths from localities worldwide (Rudnick et al., 1993; Yaxley et al., 1998; Agashev et al., 2013; Shu and Brey, 2015). However, the corresponding carbonate minerals are rarely identified in mantle xenoliths (Ionov et al., 1993, 2018; Kogarko et al., 1995; Yaxley et al., 1998; Araújo et al., 2009), compared with those documented as inclusions in diamonds (e.g. Sobolev et al., 1997, 2009a; Leost et al., 2003; Kaminsky et al., 2009 and references therein). Similarly, the record of quenched carbonatitic melts in mantle rocks is limited (van Achterbergh et al., 2002; Moine et al., 2004; Giuliani et al., 2012), whereas carbonatitic/carbonate-rich melts/fluids are commonly reported as multiphase microinclusions in fibrous diamonds (Klein-BenDavid et al., 2007, 2009; Zedgenizov et al., 2007; Logvinova et al., 2008).

Kimberlites are very rare, small-volume rocks of mantle origin that provide valuable information about melting processes and primary/primitive melts in the mantle. Kimberlite liquids originate at significant depths, 150–650 km (Mitchell, 2008; Tappe et al., 2013, 2017; Pearson et al., 2014; Sharygin et al., 2017) and possibly even deeper (Haggerty, 1994; Torsvik et al., 2010). They are traditionally classified as volatile-rich (mainly H_2O and CO_2), potassic, ultrabasic rocks. However, such deeply derived melts are unable to reach the surface unmodified due to contamination by xenogenic mantle and crustal materials, crystal fractionation and degassing. Their compositions are further transformed by ubiquitous syn/post-emplacement low-temperature alteration. Therefore, the bulk-rock compositions of kimberlites in many cases are poor indicators of their parental melt compositions. The study of fresh serpentine-free kimberlites of the Udachnaya-East pipe (Siberian craton) led to the proposal of Cl-rich alkali-

carbonatite composition of the kimberlite parental melt (Kamenetsky et al., 2008, 2012, 2014). This was further supported by compositions of melt inclusions in groundmass minerals of kimberlites worldwide (Kamenetsky et al., 2009a, 2013; Mernagh et al., 2011; Abersteiner et al., 2017).

The study of melt inclusions in minerals of mantle xenoliths is a useful method to identify compositions of mantle melts (e.g. Andersen and Neumann, 2001). Most of the melt inclusions found in mantle xenoliths are so-called 'secondary' melt inclusions. They are located along healed cracks cross-cutting the host mineral grains. The formation of such inclusions occurred after crystallisation of the host mineral grain and their existence means the presence of a melt in mantle xenoliths at some stage in their history from their initial residence in the mantle to their ejection at the surface of the Earth (e.g. Andersen and Neumann, 2001). Although there are many hypotheses for the origin of secondary melt inclusions in minerals in mantle xenoliths, the main ones are *in situ* infiltration of migrating mantle melts (i.e. mantle metasomatism model) and interaction of xenoliths with their transporting melts (e.g. Schiano and Clocchiatti, 1994; Andersen and Neumann, 2001; Golovin and Sharygin, 2007). Studies of melt inclusions in mantle xenoliths from basaltoids are numerous (e.g. review Andersen and Neumann, 2001), whereas those from kimberlites are very rare.

This study reports, for the first time, *bona fide*, secondary inclusions of crystallized alkali-rich carbonatitic melt hosted in olivine grains in sheared garnet peridotite xenoliths from the Udachnaya-East kimberlite. These xenoliths are among the most deeply derived mantle rocks available for study and originate from near the lithosphere–asthenosphere boundary (Nixon, 1995; Kennedy et al., 2002; O'Reilly and Griffin, 2010). The described inclusions are interpreted as evidence for the existence of alkali-carbonate melt in the deep mantle (≥230 km). We link these melt inclusions with the kimberlite magmatism that finally formed the Udachnaya pipe. From our point of view, the composition of the melt inclusions supports the hypothesis of the Cl-

rich, alkali-carbonatite nature of the primary/primitive kimberlite melts of the Udachnaya-East pipe.

2. Geological background

The Udachnaya pipe belongs to the Yakutian diamondiferous province (Siberian craton, Fig. 1). The pipe consists of eastern and western bodies and is hosted by Ordovician and Devonian sedimentary rocks (limestones, dolomites, marls, siltstones, mudstones, sandstones and limy conglomerates) (Kharkiv et al., 1991, 1998). The SHRIMP U-Pb perovskite age constraints suggest kimberlite emplacement at 367 ± 5 Ma for eastern body and 361 ± 4 and 353 ± 5 for different samples from western body (Kinny et al., 1997).

Each body of the Udachnaya pipe consists of several distinct kimberlite units (Kharkiv et al., 1991, 1998; Golovin et al., 2017c). All kimberlite units in the western body, as well as olivine and orthopyroxene from all mantle xenoliths, are fully serpentinised, while kimberlites below 370 m in the eastern body contain fresh olivine (Marshintsev et al., 1976; Golovin et al., 2017c). Kimberlites, free from serpentine and other secondary hydrous minerals, were found only below 410 m in the central part of the Udachnaya-East pipe (see Fig. 1 from Golovin et al., 2017c). Fresh kimberlites of the Udachnaya-East pipe are rich in alkalis (up to 8 wt% Na_2O + K_2O), chlorine (up to 6 wt%) and sulphur (up to 0.6 wt%) (Maas et al., 2005; Kamenetsky et al., 2007, 2012; Kitayama et al., 2017). They contain different alkali carbonates, sulphates, chlorides and sulphides in the groundmass (Sharygin et al., 2003, 2007a, 2007b; Kamenetsky et al., 2004; Golovin et al., 2017a) along with typical kimberlitic minerals: olivine, phlogopite, calcite, apatite and oxides (Kamenetsky et al., 2008, 2012; Chakhmouradian et al., 2013).

Serpentine-free kimberlites in the Udachnaya-East pipe contain numerous and diverse mantle xenoliths, which are also exceptionally fresh compared with those in other kimberlites of the Siberian craton (Sobolev et al., 2009b; Ionov et al., 2010, 2017; Bascou et al., 2011; Doucet

et al., 2012, 2013, 2014; Sharygin et al., 2012; Yaxley et al., 2012; Agashev et al., 2013). The sheared garnet peridotite xenoliths in this study were sampled from fresh kimberlites.

3. Sheared garnet peridotite xenolith samples

Sheared garnet peridotite xenoliths delivered to the surface by kimberlite magmas represent the deepest samples of the subcontinental lithospheric mantle. The xenoliths exhibit a porphyroclastic texture represented by large porphyroclasts of olivine, garnet and pyroxenes in a matrix of very fine-grained neoblasts (mainly olivine, less often pyroxenes) (Fig. 2). It has been proposed that the porphyroclastic texture results from recrystallization of coarse-grained peridotites under a very high-stress and high strain-rate deformation (Harte, 1977; Mercier, 1979).

Two sheared lherzolite and one harzburgite xenoliths were studied. Petrographic features and mineralogy of these rocks are summarized in Tables 1 and 2. The primary mineral assemblages of the studied samples are olivine + orthopyroxene + garnet ± clinopyroxene. The porphyroclasts (1–10 mm) and neoblasts (0.1–0.5 mm) of both olivine and pyroxene are of identical composition in the same xenolith. P-T estimates suggest that the studied xenoliths equilibrated in the mantle at 1230–1360 °C and 5.7–7.3 GPa (MacGregor, 1974; Finnerty and Boyd, 1987; Brey and Köhler, 1990), corresponding to depths of 180–230 km (see Table 1 for details). Such estimated high pressure is consistent with the presence of a majorite component in the garnet (e.g. Beyer and Frost, 2017), indicated by an excess of silicon (from 3.026 to 3.033 apfu) in the garnet formula (Table 2). Two samples are derived from 200–230 km, i.e. below the mantle region known as the ‘lithospheric diamond window’ (150–200 km) (Nixon, 1995; Stachel and Harris, 2008). The studied xenoliths do not show any low-temperature hydration, as evidenced by the absence of serpentine.

4. Methods

Petrographic studies of double-polished thin sections of the sheared garnet peridotite samples and identification of melt inclusions in rock-forming olivines from the xenoliths were done using an Olympus BX51 optical microscope combined with an Olympus COLOR VIEW III camera connected to a PC.

Chemical compositions of the rock-forming minerals were determined using a JEOL JXA-8100 electron microprobe at the Sobolev Institute of Geology and Mineralogy. The accelerating voltage was 20 kV, beam current was 40–70 nA, spot size was 2 μm and counting times for peak and for backgrounds were 10 s.

We studied both unexposed and exposed melt inclusions. Raman spectroscopy, scanning electron microscopy (SEM) coupled with energy-dispersive X-ray spectroscopy (EDS) were used for identification of daughter minerals in the inclusions. The selected inclusions were exposed to the surface of thin sections in a water-free environment using oil-based diamond pastes to avoid the loss of water-soluble minerals. After polishing, oil was removed using petroleum benzene. Nevertheless, some daughter minerals and partly fine-grained aggregates were missing in the multiphase inclusions exposed at the surface, therefore a Raman spectroscopic study of unexposed intact inclusions was the main non-destructive method.

SEM–EDS studies of exposed melt inclusions were performed using an Oxford Instruments INCA Energy 350 microanalysis system with liquid nitrogen-free Large area EDS X-Max-80 Silicon Drift Detector installed on a JEOL JSM-6510LV SEM at the Sobolev Institute of Geology and Mineralogy (SB RAS, Novosibirsk). EDS spectra were collected with an acquisition time of 60 s at an accelerating voltage of 15 kV and a beam current of 1 nA. The beam diameter was approximately 1 micron. EDS spectra were optimized for quantification using the standard XPP procedure included in the INCA Energy 350 software.

Laser-Raman spectra (from 50 to 4000 cm^{-1}) of the daughter minerals in the polyphase inclusions were collected with a Horiba Jobin Yvon T64000 dispersive Raman spectrometer using the 514.5 nm line of an Ar^+ laser with a laser power of 20 mW. The scattered Raman light was analysed with a CCD detector after being dispersed by a grating with 1800 grooves mm^{-1}. A 100× objective with a numerical aperture of 0.9 was used on a BX-51 microscope. The frequency was calibrated using the first-order Si line at 520.7 cm^{-1} and lines from a Hg lamp at 1122.5 cm^{-1}. The wavenumbers are accurate to ±1 cm^{-1}. The database of obtained Raman spectra for individual daughter minerals (larger than 5 microns in size) within the intact inclusions contains more than 100 spectra. The RRUFF database (RRUFF Project. Database of Raman Spectroscopy, X-ray Diffraction and Chemistry of Minerals. <http://rruff.info> (University of Arizona, 2012)) and published data were used for spectral identification. After the SEM study, some daughter minerals (predominantly carbonates and sulphates) were analysed again using Raman spectroscopy to obtain their 'pure' spectra without the host olivine.

Trace-element concentrations in unexposed melt inclusions (Table 3) were analysed by LA–ICP–MS at the University of Tasmania. This instrumentation comprises a New Wave Research UP213 Nd-YAG (213 nm) laser coupled to an Agilent 7500 quadrupole mass spectrometer. Analyses of inclusion clusters were performed in a He atmosphere by ablating 100–120 µm diameter spots at a rate of 10 shots/s using laser power of ~3.2 J/cm^2. The analysis time for each sample was 180 s, comprising a 30 s measurement of background (laser off) and a 150 s analysis with a laser on to allow for 'drilling' through host olivine to the inclusions at depth. The time-resolved LA–ICP–MS signal from the ablation of clusters of multiphase melt inclusions bears variable 'contributions' from different daughter minerals, so quantification of the bulk composition requires integration of signal intensities over the entire interval of inclusion ablation. Data reduction was undertaken according to standard methods (Longerich et al., 1996) using the NIST612 and USGS BCR-2G glasses as primary and secondary reference materials, respectively. The background values were taken from the analyses of host olivine, devoid of any

inclusions, at the conditions (laser spot) of the analysis. In the absence of the internal standard, all the data reported below represent relative values or element ratios that are sufficient to trace principal geochemical characteristics (e.g. relative enrichment of alkali elements over Ca or light rare-earth elements over heavy rare-earth elements). Average compositions of melt inclusions were obtained for two samples: UV-1/03 (12 analyses) and UV-67/03 (six analyses) (Table 3).

Heating experiments with melt inclusions were performed in the Sobolev Institute of Geology and Mineralogy SB RAS using a heating stage (Osorgin and Tomilenko, 1990, USSR Inventor's Certificate no. 1592678) installed on an Olympus BX51 microscope. A Linkam THMS 600 heating/cooling stage was used to study the behaviour of melt inclusions from +20 to –195 °C.

5. Results

All studied xenoliths contain secondary melt inclusions (≤100 μm across) that were trapped in randomly oriented healed fractures in both olivine porphyroclasts and neoblasts (Fig. 3A). Occasionally, healed cracks continue from porphyroclasts into neoblasts. The multiphase inclusions are composed of bubble(s), well-defined crystals and fine-grained aggregates (Fig. 3B). The assemblage of daughter minerals is the same in inclusions located in porphyroclasts and in neoblasts.

SEM–EDS (Fig. 3C–F and Suppl. Fig. 1) and Raman spectroscopy (Fig. 4–6) demonstrate that daughter minerals are represented by a large variety of Na-K-Ca-, Na-Ca-, Na-Mg-, Ca-Mg- and Ca-carbonates, Na-Mg-carbonates with additional anions, K-Na- and Na-sulphates, Na-, K-, Mg-halides, K-Fe-Ni-, K-Fe-, Fe-Ni- and Fe-sulphides, phosphates, oxides and silicates: nyerereite, pure $Na_2Ca(CO_3)_2$ phase, shortite, eitelite, northupite, bradleyite, tychite, burkeite, dolomite, aragonite, calcite, aphthitalite, halite, sylvite, chloromagnesite, pyrrhotite, pentlandite, djerfisherite, rasvumite, apatite, perovskite, chromite, Ti-magnetite,

magnetite, ilmenite, rutile, tetraferriphlogopite, phlogopite, olivine, diopside, sodalite and richterite (Table 4). The fine-grained aggregates are composed of alkali carbonates, sulphates and chlorides with the grain size ≤1 μm.

5.1. Raman spectroscopic study of daughter minerals

Aragonite $CaCO_3$ (Fig. 4A) was identified by the following diagnostic Raman bands: strong band at 1086 cm^{-1}, three medium bands at 153, 208 and 704 cm^{-1}, three weak bands at 181, 191 and 1464 cm^{-1} (Edwards et al., 2005; RRUFF database).

In contrast to aragonite, calcite $CaCO_3$ (Fig. 4B) has the following diagnostic Raman bands: strong band at 1086 cm^{-1}, three medium bands at 153, 281 and 713 cm^{-1}, a weak band at 1436 cm^{-1} (Edwards et al., 2005; RRUFF database).

Dolomite $CaMg(CO_3)_2$ (Fig. 4C) was identified by the following diagnostic Raman bands: strong band at 1098 cm^{-1}, two medium bands at 176 and 300 cm^{-1}, weak bands at 725 and 1442 cm^{-1} (Edwards et al., 2005; RRUFF database).

Nyerereite $(Na,K)_2Ca(CO_3)_2$ (Fig. 4D) has one strong band at 1085–1089 cm^{-1} with a weak shoulder at 1077–1079 cm^{-1} in its Raman spectra. It may also have up to three medium/weak bands at 683–689, 710–711 and 726–727 cm^{-1} in the 670–730 cm^{-1} region (Zaitsev et al., 2009; Golovin et al., 2015, 2017b).

Potassium-poor $Na_2Ca(CO_3)_2$ carbonate (Fig. 4E), which has a different structure from nyerereite, was also identified within the melt inclusions by two strong bands at 1072–1073 and 1086–1087 cm^{-1} in its Raman spectra (Gavryushkin et al., 2016; Bolotina et al., 2017; Golovin et al., 2017b).

The Raman spectra of shortite $Na_2Ca_2(CO_3)_3$ (Fig. 4F–H) displays two strong bands at 1071–1075 and 1090–1093 cm^{-1} and several medium/weak bands in the region 680–740 cm^{-1} (Frost and Dickfos, 2008; Golovin et al., 2017c; RRUFF database).

The Raman spectra of eitelite $Na_2Mg(CO_3)_2$ (Fig. 4G) are characterized by a strong band at 1105–1106 cm^{-1} and weaker bands at 207–209 and 260–263 cm^{-1} (Shatskiy et al., 2013; RRUFF database).

The Raman spectra of northupite $Na_3Mg(CO_3)_2Cl$ (Fig. 4H) display up to eight strong/medium bands at 121, 180, 214, 250, 305, 715, 1106 and 1116 cm^{-1} (RRUFF database).

Bradleyite $Na_3Mg(PO_4)(CO_3)$ (Fig. 4I) was identified by two strong bands at 971 and 1078 cm^{-1} and two medium bands at 218 and 591 cm^{-1} in its Raman spectra (Gao et al., 2015).

The Raman spectra of tychite $Na_6Mg_2(SO_3)(CO_3)_4$ (Fig. 4J) display two strong bands at 967 and 1110 cm^{-1} and up to eight weak bands at 212, 250, 297, 465, 631, 713, 1170 and 1134 cm^{-1} (RRUFF database).

The Raman spectra of burkeite $Na_6(CO_3)(SO_4)_2$ (Fig. 4K) are characterized by two strong bands at 993 and 1066 cm^{-1}, up to eight medium bands at 452, 477, 619, 632, 644, 1102 and 1133 cm^{-1}, a weak band at 705 cm^{-1} (RRUFF database).

In addition, we could not identify some daughter minerals (e.g. Fig. 4I) with Raman bands in the regions attributed to CO_3^{2-} and SO_4^{2-} vibrations because of the lack of reference Raman spectra.

Aphthitalite $K_3Na(SO_4)_2$ (Fig. 5) has the following diagnostic Raman bands: strong band at 992 cm^{-1}, two medium bands at 452 and 620 cm^{-1}, weak bands at 161, 627, 1082 and 1203 cm^{-1} (RRUFF database).

The following bands occur in the Raman spectra of tetraferriphlogopite $KMg_3FeSi_3O_{10}(F,Cl,OH)$ (Fig. 6A): two strong bands at 92 and 179 cm^{-1}, up to seven medium bands at 353, 679, 714, 741, 935, 961 and 1044 cm^{-1}, broad OH band at 3706 cm^{-1} (Korsakov et al., 2014).

Richterite $Na_2Ca(Mg,Fe)_5Si_8O_{22}(OH)_2$ (Fig. 6B) are characterized by a strong band at 681 cm^{-1}, two medium bands at 223 and 1078 cm^{-1}, up to eight weak bands at 107, 300, 334, 368, 395, 519 and 591 cm^{-1} (RRUFF database).

5.2. Heating and cooling experiments with melt inclusions

The experimental study demonstrated that during cooling to –195 °C, no phase changes occur in the melt inclusions, suggesting the absence of a fluid phase (gas and/or liquid CO_2 and/or H_2O). The Raman spectroscopy study of shrinkage bubbles did not detect any free volatile phase.

Heating experiments showed that extensive melting of the daughter minerals assemblage of the melt inclusions starts at 500–560 °C, followed by decrepitation at 650–850 °C (Fig. 7). The melt within inclusions formed a fine-grained aggregate upon quenching. This aggregate disintegrated in exposed melt inclusions and was not suitable for electron probe microanalysis.

5.3. Chemical composition of melt inclusions

The average Na:K:Ca molar ratio of the melt inclusions is 2.2:1.2:1 (Fig. 8A). The lithophile trace-element compositions of the melt inclusions were averaged (Table 3) and normalized to the composition of the primitive mantle (McDonough and Sun, 1995; Fig. 8B). The abundances of fluid-mobile Rb, Ba, K, Pb and Sr in the melt inclusions are high, and these elements are enriched relative to the immobile elements of similar incompatibility (e.g. Th, La and Pr).

The presence of 17 alkali-rich species among a total of 32 identified minerals within the melt inclusions reflects their high bulk alkali contents. Examination of unexposed and exposed melt inclusions using optical microscopy (Fig. 9), scanning electron (Fig. 3C–F and Suppl. Fig. 1) microscopy and Raman spectroscopy (Fig. 4–6) revealed that carbonate, chloride and sulphate minerals are predominant among the daughter minerals; other minerals are present in subordinate amounts. Thus, parental melt for inclusions are Cl–S-rich alkali-carbonate melt.

6. Discussion

6.1. Composition of the secondary melt inclusions

High-pressure experiments have demonstrated that the low degree of partial melting of even alkali-poor carbonated peridotite and eclogite systems produced alkali-rich carbonatite melts (e.g. Wallace and Green, 1988; Kiseeva et al., 2012, 2013; Dasgupta et al., 2013; Litasov et al., 2013; Thomson et al., 2016). The melt inclusions described here may be natural analogues of such experimentally observed melts. The 'snapshots' of olivine-hosted melts in the sheared garnet peridotite xenoliths have alkali-carbonatitic compositions, identified in our study by (1) numerous alkali-rich daughter minerals (17 among a total of 32); (2) high (Na + K)/Ca bulk molar ratio ~3.4; (3) abundance of carbonate minerals; (4) phase transformations observed on heating and cooling. Moreover, the mineralogy of the crystallized melt inclusions (Table 4) is similar to that of the alkali-rich carbonate melt inclusions in minerals from carbonatites (Veksler et al., 1998; Veksler and Lentz; 2006; Campeny et al., 2015).

6.2. Genesis of the secondary melt inclusions

Natrocarbonatite lavas of the active Oldoinyo Lengai volcano (Gregory Rift, northern Tanzania) represent the only known alkali-carbonate melt erupted at the Earth's surface where Na + K >> Ca. However, the melt recorded in the current study (in at%, Na:K:Ca – 2.2:1.2:1) is distinctly less alkaline than the Oldoinyo Lengai lavas (in at%, Na:K:Ca – 3.6:0.6:1) (Keller and Zaitsev, 2012). On the other hand, the studied melt inclusions fall within the field of alkali-carbonatite microinclusions in fibrous diamonds on the Na–K–Ca ternary diagram, suggesting a possible genetic link (Fig. 8A). High-pressure experimental studies demonstrated that alkali carbonate melts have been previously implicated as a diamond-forming medium, with the most effective environment for diamond nucleation and growth at the *P–T* conditions (5–6 GPa, 900–1400 °C) of the subcratonic lithosphere mantle (e.g. Pal'yanov et al., 1999; Palyanov and Sokol, 2009). Therefore, both studied melt inclusions in olivine from the sheared peridotites and

microinclusions reported in fibrous diamonds testify to the existence of a distinctive reservoir of alkali-carbonatite melts in the deep cratonic mantle.

It is also worth noting that the melt inclusions in peridotitic olivine are broadly similar to melt inclusions in phenocrystic olivine from the host Udachnaya-East kimberlites in terms of their daughter mineral assemblages (Table 4), trace-element compositions and their behaviour upon quenching after heating (Golovin et al., 2003, 2007; Kamenetsky et al., 2004, 2009a). The groundmass of host kimberlites contains the same magmatic alkaline carbonates, sulphates, sulphides and halides (Table 4). Thus, we infer genetic relationships between the alkali-carbonate melts, which interacted with sheared peridotites and kimberlite magmatism. However, the high-pressure polymorph of $CaCO_3$, aragonite, identified in our study, was not found among either groundmass minerals nor daughter minerals in melt inclusions in phenocrystic olivine (see Table 4 and Golovin et al. (2007), Mernagh et al. (2011) and Tomilenko et al. (2017)).

6.3. Nature and depth of formation of the secondary melt inclusions: scenarios

Deformation microstructures of the sheared peridotites could not be preserved for more than a few years during annealing at the temperatures recorded by their mineral chemistry (Mercier, 1979; Drury and van Roermund 1989; O'Reilly and Griffin, 2010). This means that both deformation and subsequent recrystallization of the peridotites were linked in time with the magmatism that finally erupted kimberlites. The presence of the same secondary melt inclusions both in porphyroclasts and neoblasts of olivines indicates that infiltration of melt along fractures occurred after deformation of the studied peridotites. Therefore, the formation of melt inclusions in olivine of sheared peridotites from Udachnaya-East pipe could be temporally connected with kimberlite magmatism.

Two plausible scenarios for the formation of the melt inclusions in the sheared peridotite xenoliths can be considered. The first scenario is infiltration of the kimberlite melt into entrapped xenoliths during magma ascent. Drury and van Roermund (1989) demonstrated that

recrystallization during annealing of sheared peridotite after deformation occurs in the presence of intergrain melt and this melt most probably was derived from the kimberlite during uplift of the xenolith. On the basis of numerical calculations, Brett et al. (2015) estimated that peridotitic olivine grains start to develop internal cracks after 15–25 km from the entrapment level at the ascent velocities of 0.1 to >4 m s−1 expected for kimberlite magma. In case of the studied xenoliths (entrapment level 230–180 km) olivine cracking could occur at depths of ~210–160 km. Because carbonatite melt has low viscosity and appropriate wetting properties, its infiltration into olivine grains and entrapment as melt inclusions would occur almost simultaneously with olivine cracking. Therefore, the melt within the inclusions in olivine of the sheared peridotites xenoliths would represent primitive or slightly evolved kimberlite melt.

The second scenario is percolation of the immediate precursor of kimberlite melt, i.e. melt that segregated from the top of kimberlite melt generation region at the pre-eruption stage, through peridotite *in situ.* This may be evidenced by the following. Trace-element zoning of garnets from some sheared peridotite xenoliths from South African kimberlites indicates the reaction between the garnets and infiltrating melt (Griffin et al., 1989, 1996). A simple calculation using diffusion rates has shown that observed zoning profiles form during a time range from a few days to hundreds of years (Griffin et al., 1996). Thus, on the basis of these results, Griffin et al. (1989, 1996) concluded that the melt percolation through sheared peridotites was connected with their deformation and occurred shortly before eruptions of the kimberlite magma. Therefore, kimberlite melt that segregated from the source region at the pre-eruption stage is a good candidate for this infiltrating melt. This melt was usually termed protokimberlite melt (e.g. Griffin et al., 1989). Note, Zr/Y is 1 to 2 in garnet cores but 4 to 5 in rims, which was interpreted to mean that the infiltrating melt had high Zr/Y (Griffin et al., 1989). This scenario may be considered in our case because some garnet grains from sheared peridotites from the Udachnaya-East kimberlite pipe demonstrate the same zoning pattern (e.g. Agashev et al., 2013). In particular, garnet from one of the studied samples, UV-3/05, has Zr/Y = 2.5 in the

core and Zr/Y = 8.4 in the rim (Agashev et al., 2013). The alkali-carbonatite melt inclusions described here have high bulk Zr/Y = 6–9 (Table 3) and, thus, could represent infiltrating melt as suggested by Griffin et al. (1989). Because sheared peridotites are the deepest xenoliths derived by kimberlite melt, they can be closest to the kimberlite melt source region and thus this infiltrating melt may be compositionally similar to primary kimberlite melt. According to Drury and van Roermund (1989), cracking of olivine in sheared peridotites can even exist during deformation *in situ*. This infiltrating melt could form secondary melt inclusions in olivine of sheared peridotites *in situ* or during ascent after 15–25 km from the entrapment level according to the numerical model of Brett et al. (2015). Therefore, the melt hosted by olivine of sheared peridotites may be an immediate precursor of kimberlite melt and close-to-primary or primitive in composition.

The presence of aragonite amongst the daughter minerals in the melt inclusions (Fig. 4A) in all studied xenoliths is well integrated into both scenarios**.** According to experimental data (Irving and Wyllie, 1975) aragonite is a reliable geobarometer that is routinely used in studies of magmatic and ultrahigh-pressure metamorphic rocks as an indicator of high pressures (Korsakov and Hermann, 2006; Korsakov et al., 2009; Humphreys et al., 2010). Moreover, recent experimental studies of melting phase relations demonstrated that aragonite is stable in carbonate, alkali-carbonate and alkali-rich carbonate–silicate systems at upper mantle pressures and temperatures (Litasov et al., 2013; Sharygin et al., 2015; Shatskiy et al., 2015). Note that evidence of metastable crystallization of aragonite in the calcite stability field during magmatic processes is currently lacking. Similarly, in our study, daughter aragonite provides strong support for a mantle origin for the studied melt inclusions. The shallowest level for aragonite to form in the melt inclusions should be at >120 km depth (Fig. 10), considering *P–T* pathways of kimberlite magma ascent (Kavanagh and Sparks, 2009). The presence of aragonite and calcite in different individual inclusions belonging to the same trail may be explained by crystallization of individual phases inside inclusions starting at mantle levels in the aragonite stability field and

proceeding into the calcite stability field until ~500 °C (i.e. solidus of melt inclusions). Alternatively, melt inclusions in olivine from xenoliths can retain enough residual internal pressure for aragonite crystallization even when the kimberlite magma is at depths within the calcite stability field.

It is well known that in various peridotite – carbonate, olivine – carbonate and orthopyroxene – carbonate systems, which may serve as models for kimberlite magma, there is no free fluid CO_2 phase at pressures >2–3 GPa (Wyllie and Huang, 1975; Wallace and Green, 1988; Falloon and Green, 1989; Kamenetsky and Yaxley, 2015; Stone and Luth, 2016, Sharygin et al., 2017). However, at pressures <2–3 GPa, interaction of silicates, especially orthopyroxene, with carbonatite melt produces a free fluid CO_2 phase in these systems (Wyllie and Huang, 1975; Wallace and Green, 1988; Falloon and Green, 1989; Russell et al., 2012; Stone and Luth, 2016).

Free fluid CO_2 was found both as fluid inclusions and as bubbles in crystallized secondary melt inclusions in some olivine phenocryst/microphenocryst from Udachnaya-East kimberlites (Sobolev et al., 1989; Golovin et al., 2003, 2007; Kamenetsky et al., 2008; Kamenetsky and Yaxley, 2015). This indicated that the free fluid CO_2 phase may really be present in kimberlite magma at <2–3 GPa at the time of inclusion formation. In our case, the lack of free fluid CO_2 phase in secondary melt inclusions from olivines of sheared peridotite xenoliths indicates that free fluid CO_2 phase was absent in the peridotite – carbonatite melt system at the time of inclusion formation. Thus, this may support an origin as secondary melt inclusions from olivines of sheared peridotites at pressure >2–3 GPa (>70–100 km), i.e. may serve as additional indirect evidence for the mantle origin of these inclusions.

Regardless of the considered scenarios, the infiltration of Cl–S-bearing alkali-carbonate melts into sheared peridotites resulted in the secondary melt inclusion formation taking place at mantle depths between 230 and 120 km. The minimum depth of secondary melt inclusions formation is estimated taking into account the *P–T* pathway of kimberlite magma ascent (Kavanagh and Sparks, 2009) and calcite–aragonite phase boundary (Irving and Wyllie, 1975).

The parental melt for secondary melt inclusions came from below the sheared peridotites entrapment level, i.e. it originated at depths greater than 230 km.

7. Concluding remarks

In this paper we provide detailed description of secondary melt inclusions in sheared peridotite xenoliths derived from 180–230 km depths. It was found that the melt inclusions contain alkali-rich carbonates, halides and sulphates, which are predominant among the daughter minerals, and aragonite, a high-pressure polymorph of $CaCO_3$. This study is evidence of the existence of Cl–S-rich alkali-carbonatite melt in deep mantle > 230 km beneath Siberian craton.

At present, the unaltered kimberlites of the Udachnaya-East pipe are a unique example of the Na-, Cl-rich and H_2O-poor kimberlite magma. Contrary to the generally accepted ultramafic silicate nature of kimberlite melts, at least some primary/primitive kimberlite melts are now considered to be alkali-carbonate liquids (Kamenetsky et al., 2007, 2008, 2012, 2014; Russell et al., 2012; Sharygin et al., 2015; Shatskiy et al., 2017). Evolution of the original carbonatite melt towards common ultramafic kimberlite is attributed to chemical contamination by, and mechanical incorporation of, the xenogenic mantle silicates (e.g. Kamenetsky et al., 2008, 2009b; Brett et al., 2009; Russell et al., 2012; Stone and Luth, 2016; Sharygin et al., 2017).

The genetic link between alkali-carbonate melt inclusions in olivine of sheared peridotite xenoliths and kimberlite magmatism, recognized in this study, is further conclusive evidence in support of the alkali-carbonatitic composition of primary/primitive kimberlite melts of the Udachnaya pipe.

Acknowledgements

We thank K. Kiseeva, S. Tappe and E.-R. Neumann for their constructive and thoughtful comments and K. Kiseeva for editorial handling. AVG and AVK were supported by the Russian Federation state assignment project No. 0330-2016-0006. ISS was supported by the Russian

Foundation for Basic Research (grant No. 16-35-60052 mol_a_dk) and the Ministry of Education and Science of the Russian Federation through the research grant program of the President of the Russian Federation for young Russian scientists (grant No. MK-4534.2016.5).

References

Abersteiner, A., Giuliani, A., Kamenetsky, V.S., Phillips, D., 2017. Petrographic and melt inclusion constraints on the petrogenesis of a magmaclast from the Venetia kimberlite cluster, South Africa. Chem. Geol. 455, 326–336.

Agashev, A.M., Ionov, D.A., Pokhilenko, N.P., Golovin, A.V., Cherepanova, Y., Sharygin, I.S., 2013. Metasomatism in lithospheric mantle roots: Constraints from whole-rock and mineral chemical composition of deformed peridotite xenoliths from kimberlite pipe Udachnaya. Lithos 160-161, 201–215.

Andersen, T., Neumann, E.-R., 2001. Fluid inclusions in mantle xenoliths. Lithos 55, 301–320.

Araújo, D.P., Griffin, W.L., O'Reilly, S.Y., 2009. Mantle melts, metasomatism and diamond formation: Insights from melt inclusions in xenoliths from Diavik, Slave Craton. Lithos 112, 675–682.

Bascou, J., Doucet, L.S., Saumet, S., Ionov, D.A., Ashchepkov, I.V., Golovin, A.V., 2011. Seismic velocities, anisotropy and deformation in Siberian cratonic mantle: EBSD data on xenoliths from the Udachnaya kimberlite. Earth Planet. Sci. Lett. 304, 71–84.

Beyer, C., Frost, D.J., 2017. The depth of sub-lithospheric diamond formation and the redistribution of carbon in the deep mantle. Earth Planet. Sci. Lett. 461, 30–39.

Bolotina, N.B, Gavryushkin, P.N., Korsakov, A.V., Rashchenko, S.V., Seryotkin, Y.V., Golovin, A.V., Moine, B.N., Zaitsev, A.N., Litasov, K.D., 2017. Incommensurately modulated twin structure of nyerereite $Na_{1.64}K_{0.36}Ca(CO_3)_2$. Acta Crystallogr. B 73, 276–284.

Boullier, A.M., Nicolas, A., 1975. Classification of texture and fabric of peridotite xenoliths from South African kimberlits. Phys. Chem. Earth 9, 467–476.

Brett, R., Russell, J., Andrews, G., Jones, T, 2015. The ascent of kimberlite: Insights from olivine. Earth Planet. Sci. Lett. 424, 119–131.

Brey, G.P., Köhler, T., 1990. Geothermobarometry in four-phase lherzolites II. New thermobarometers, and practical assessment of existing thermobarometers. J. Petrol. 31, 1353–1378.

Campeny, M., Kamenetsky, V.S., Melgarejo, J.C., Mangas, J., Manuel, J., Alfonso, P., Kamenetsky, M.B., Bambi, A.C.J.M., Gonçalves, A.O., 2015. Carbonatitic lavas in Catanda (Kwanza Sul, Angola): Mineralogical and geochemical constraints on the parental melt: Lithos 232, 1–11.

Chakhmouradian, A.R., Reguir, E.P., Kamenetsky, V.S., Sharygin, V.V., Golovin, A.V., 2013. Trace-element partitioning in perovskite: implications for the geochemistry of kimberlites and other mantle-derived undersaturated rocks. Chem. Geol. 353, 112-131.

Dalton, J.A., Wood, B.J, 1993. The compositions of primary carbonate melts and their evolution through wallrock reaction in the mantle. Earth Planet. Sci. Lett. 119, 511–525.

Dasgupta, R., Mallik, A., Tsuno, K., Withers, A.C., Hirth, G., and Hirschmann, M.M., 2013, Carbon-dioxide-rich silicate melt in the Earth's upper mantle. Nature 493, 211–215.

Doucet, L.S., Ionov, D.A., Golovin, A.V., Pokhilenko, N.P., 2012. Depth, degrees and tectonic settings of mantle melting during craton formation: inferences from major and trace element compositions of spinel harzburgite xenoliths from the Udachnaya kimberlite, central Siberia. Earth Planet. Sci. Lett. 359–360, 206–218.

Doucet, L.S., Ionov, D.A., Golovin, A.V., 2013. The origin of coarse garnet peridotites in cratonic lithosphere: new data on xenoliths from the Udachnaya kimberlite, central Siberia. Contrib. Mineral. Petrol. 165, 1225–1242.

Doucet, L.S., Peslier A.H., Ionov D.A., Brandon A.D., Golovin A.V., Goncharov A.G., Ashchepkov I.V., 2014. High water contents in the Siberian cratonic mantle linked to metasomatism: an FTIR study of Udachnaya peridotite xenoliths. Geochim. Cosmochim. Acta 137, 159–187.

Drury, M.R., van Roermund, H.L.M., 1989. Fluid assisted recrystallization in upper mantle peridotite xenoliths from kimberlites. J. Petrol. 30, 133–152.

Dziewonski, A.M., Anderson, D.L., 1981. Preliminary reference Earth model. Phys. Earth Planet. In. 25, 297–356.

Edwards, H.G.M., Villar, S.E.J., Jehlicka, J., and Munshi, T., 2005. FT-Raman spectroscopic study of calcium-rich and magnesium-rich carbonate minerals. Spectrochim. Acta A 61, 2273–2280.

Falloon, T.J., Green, D.H., 1989. The solidus of carbonated, fertile peridotite. Earth Planet. Sci. Lett. 94, 364–370.

Finnerty, A.A., Boyd, F.R., 1987. Thermobarometry for garnet peridotites: basis for the determination of thermal and compositional structure of the upper mantle. Pp. 381–402 in: Mantle Xenoliths. Chichester: John Wiley & Sons.

Frost, R.L., Dickfos, M.J., 2008. Raman and infrared spectroscopic study of the anhydrous carbonate minerals shortite and barytocalcite. Spectrochim. Acta A 71, 143–146.

Gao, J., Huang, W., Wu, X., Fan, D., Wu, Z., Xia, D., Qin, S., 2015. Compressibility of carbonophosphate bradleyite $Na_3Mg(CO_3)(PO_4)$ by X-ray diffraction and Raman spectroscopy. Phys. Chem. Miner. 42, 191–201.

Gavryushkin, P.N., Thomas, V.G., Bolotina, N.B., Bakakin, V.V., Golovin, A.V., Seryotkin, Y.V., Fursenko, D.A., Litasov, K.D., 2016. Hydrothermal synthesis and structure solution of $Na_2Ca(CO_3)_2$: “synthetic analogue” of mineral nyerereite. Cryst. Growh Des. 16, 1893–1902.

Giuliani, A., Kamenetsky, V.S., Phillips, D., Kendrick, M.A., Wyatt, B.A., Goemann, K., 2012. Nature of alkali-carbonate fluids in the sub-continental lithospheric mantle. Geology 40, 967–970.

Golovin, A.V., Sharygin, V.V., Pokhilenko, N.P., Mal'kovets, V.G., Kolesov, B.A., Sobolev, N.V., 2003. Secondary melt inclusions in olivine from unaltered kimberlites of the Udachnaya-East pipe, Yakutia. Dokl. Earth Sci. 388, 93–96.

Golovin, A.V., Sharygin, V.V., 2007. Petrogenetic analysis of fluid and melt inclusions in minerals from mantle xenoliths from the Bele pipe basanites (North Minusa depression). Russ. Geol. Geophys. 48, 811–824.

Golovin, A.V., Sharygin, V.V., Pokhilenko, N.P., 2007. Melt inclusions in olivine phenocrysts in unaltered kimberlites from the Udachnaya-East pipe, Yakutia: some aspects of kimberlite magma evolution during late crystallization stages. Petrology 15, 168–183.

Golovin, A.V., Korsakov, A.V., Zaitsev, A.N., 2015. In situ ambient and high-temperature Raman spectroscopic studies of nyerereite $(Na,K)_2Ca(CO_3)_2$: can hexagonal zemkorite be stable at earth-surface conditions? J. Raman Spectrosc. 46, 904−912.

Golovin, A.V., Goryainov, S.V., Kokh, S.N., Sharygin, I.S., Rashchenko, S.V., Kokh, K.A., Sokol, E.V., Devyatiyarova, A.S., 2017a. The application of Raman spectroscopy to djerfisherite identification. // J. Raman Spectrosc. 48, 1574−1582.

Golovin, A.V., Korsakov, A.V., Gavryushkin, P.N., Zaitsev, A.N., Thomas, V.G., Moine, B.N., 2017b. Raman spectra of nyerereite, gregoryite and synthetic pure $Na_2Ca(CO_3)_2$: diversity and application for the study micro inclusions. J. Raman Spectrosc. 48, 1559−1565.

Golovin, A.V., Sharygin, I.S., Korsakov, A.V., 2017c. Origin of alkaline carbonates in kimberlites of the Siberian craton: Evidence from melt inclusions in mantle olivine of the Udachnaya-East kimberlite. Chem. Geol. 455, 357−375.

Griffin, W.L., Smith, D., Boyd F.R., Cousens, D.R., Ryan C.G., Sie, S.H., Suter G.F., 1989. Trace-element zoning in garnets from sheared mantle xenoliths. Geochim. Cosmochim. Acta 53, 561–567.

Griffin, W.L., Smith, D., Ryan, C.G., O'Reilly, S.Y., Win, T.T., 1996. Trace-element zoning in mantle minerals: metasomatism and thermal events in the upper mantle. Can. Mineral. 34, 1179–1193.

Haggerty, S.E., 1994. Superkimberlites: A geodynamic diamond window to the Earth's core. Earth Planet. Sci. Lett. 122, 57–69.

Harte, B., 1977. Rock nomenclature with particular relation to deformation and recrystallisation textures in olivine-bearing xenoliths. Geology 85, 279–288.

Humphreys, E.R., Bailey, K., Hawkesworth, C.J., Wall, F., Najorka, J., Rankin, A.H., 2010. Aragonite in olivine from Calatrava, Spain – Evidence for mantle carbonatite melts from > 100 km depth. Geology 38, 911−914.

Ionov, D.A., Dupuy, C., O'Reilly, S.Y., Kopylova, M.G., Genshaft, Y.S., 1993. Carbonated peridotite xenoliths from Spitsbergen: implications for trace element signature of mantle carbonate metasomatism. Earth Planet. Sci. Lett. 119, 283–297.

Ionov, D., Doucet, L., Ashchepkov, I., 2010. Composition of the lithospheric mantle in the Siberian craton: new constraints from fresh peridotites in the Udachnaya-East kimberlite. J. Petrol. 51, 2177–2210.

Ionov, D.A., Doucet, L.S., Pogge von Strandmann, P.A.E., Golovin, A.V., Korsakov, A.V., 2017. Links between deformation, chemical enrichments and Li-isotope compositions in the lithospheric mantle of the central Siberian craton. Chem. Geol. 475, 105–121.

Ionov, D.A., Doucet, L.S., Xu, Y., Golovin, A.V., Oleinikov, O.B., 2018. Reworking of Archean mantle in the NE Siberian craton by carbonatite and silicate melt metasomatism: Evidence from a carbonate-bearing, dunite-to-websterite xenolith suite from the Obnazhennaya kimberlite. Geochim. Cosmochim. Acta, https://doi.org/10.1016/j.gca.2017.12.028.

Irving, A.J., Wyllie, P.J., 1975. Subsolidus and melting relationships for calcite, magnesite and the join $CaCO_3$-$MgCO_3$ to 36 kbar. Geochim. Cosmochim. Acta 39, 35–53.

Kamenetsky, M.B., Sobolev, A.V., Kamenetsky, V.S., Maas, R., Danyushevsky, L.V., Thomas, R., Pokhilenko, N.P., Sobolev, N.V., 2004. Kimberlite melts rich in alkali chlorides and carbonates: a potent metasomatic agent in the mantle. Geology 32, 845–848.

Kamenetsky, V.S., Kamenetsky, M.B., Sharygin, V.V., Golovin, A.V., 2007. Carbonate-chloride enrichment in fresh kimberlites of the Udachnaya-East pipe, Siberia: a clue to physical properties of kimberlite magmas? Geophys. Res. Lett. 34, L09316. http://dx.doi.org/10.1029/2007GL029389.

Kamenetsky, V.S., Kamenetsky, M.B., Sobolev, A.V., Golovin, A.V., Demouchy, S., Faure, K., Sharygin, V.V., Kuzmin, D.V., 2008. Olivine in the Udachnaya-East kimberlite (Yakutia, Russia): types, compositions and origins. J. Petrol. 49, 823–839.

Kamenetsky, V.S., Kamenetsky, M.B., Weiss, Y., Navon, O., Nielsen, T.F.D., Mernagh, T.P., 2009a. How unique is the Udachnaya-East kimberlite? Comparison with kimberlites from the Slave Craton (Canada) and SW Greenland. Lithos 112, 334–346.

Kamenetsky, V.S., Kamenetsky, M.B., Sobolev, A.V., Golovin, A.V., Sharygin, V.V., Pokhilenko, N.P., Sobolev, N.V., 2009b. Can pyroxenes be liquidus minerals in the kimberlite magma? Lithos 112, 213–222.

Kamenetsky, V.S., Kamenetsky, M.B., Golovin, A.V., Sharygin, V.V., Maas, R., 2012. Ultra-fresh salty kimberlite of the Udachnaya–East pipe (Yakutia, Russia): a petrological oddity or fortuitous discovery? Lithos 152, 173–186.

Kamenetsky, V.S., Grütter, H., Kamenetsky, M.B., Gömann, K., 2013. Parental carbonatitic melt of the Koala kimberlite (Canada): constraints from melt inclusions in olivine and Cr-spinel, and groundmass carbonate. Chem. Geol. 353, 96–111.

Kamenetsky, V.S., Golovin, A.V., Maas, R., Giuliani, A., Kamenetsky, M.B., Weiss, Y., 2014. Towards a new model for kimberlite petrogenesis: evidence from unaltered kimberlites and mantle minerals. Earth Sci. Rev. 139, 145–167.

Kamenetsky, V. S., Yaxley, G. M., 2015. Carbonate–silicate liquid immiscibility in the mantle propels kimberlite magma ascent. Geochim. Cosmochim. Acta 158, 48–56.

Kaminsky, F., Wirth, R., Matsyuk, S., Schreiber, A., Thomas, R., 2009. Nyerereite and nahcolite inclusions in diamond: evidence for lower-mantle carbonatitic magmas. Mineral. Mag. 73, 797−816.

Kavanagh, J. L., Sparks, R. S. J, 2009. Temperature changes in ascending kimberlite magma. Earth Planet. Sci. Lett. 286, 404–413.

Keller, J., Zaitsev, A.N., 2012. Geochemistry and petrogenetic significance of natrocarbonatites at Oldoinyo Lengai, Tanzania: Composition of lavas from 1988 to 2007. Lithos 148, 45–53.

Kennedy, L.A., Russell, J.K., Kopylova, M.G., 2002. Mantle shear zones revisited: The connection between the cratons and mantle dynamics. Geology 30, 419–422.

Kharkiv, A.D., Zuenko, V.V., Zinchuk, N.N., Kryuchkov, A.I., Ukhanov, A.V., Bogatykh, M.V., 1991. Petrochemistry of Kimberlites [in Russian]. Nedra, Moscow (304 pp.).

Kharkiv, A.D., Zinchuk, N.N., Kruchkov, A.I., 1998. Primary Diamond Deposits of the World [in Russian]. Nedra, Moscow (555 pp.).

Kinny, P.D., Griffin,W.L., Heaman, L.M., Brakhfogel, F.F., Spetsius, Z.V., 1997. SHRIMP U–Pb ages of perovskite from Yakutian kimberlites. Russ. Geol. Geophys. 38, 91–99.

Kiseeva, E.S., Yaxley, G.M., Hermann, J., Litasov, K.D., Rosenthal, A., Kamenetsky, V.S., 2012. An experimental study of carbonated eclogite at 3.5-5.5 GPa: Implications for silicate and carbonate metasomatism in the cratonic mantle. J. Petrol. 53, 727–759.

Kiseeva, E.S., Litasov, K.D., Yaxley, G.M., Ohtani, E., Kamenetsky, V.S., 2013. Melting and phase relations of carbonated eclogite at 9–21 GPa and the petrogenesis of alkali-rich melts in the deep mantle. J. Petrol. 54, 1555–1583.

Kitayama Y., Thomassot E., Galy A., Golovin A., Korsakov A., d'Eyrames E., Assayag N., Bouden N., Ionov D., 2017. Co-magmatic sulfides and sulfates in the Udachnaya-East pipe (Siberia): A record of the redox state and isotopic composition of sulfur in kimberlites and their mantle sources. Chem. Geol. 455, 315–330.

Klein-Ben David, O., Izraeli, E. S., Hauri, E. & Navon, O, 2007. Fluid inclusions in diamonds from the Diavik mine, Canada and the evolution of diamond-forming fluids. Geochim. Cosmochim. Acta 71, 723–744.

Klein-BenDavid, O., Logvinova, A.M., Schrauder, M., Spetius, Z.V., Weiss, Y., Hauri, E.H., Kaminsky, F.V., Sobolev, N.V., Navon, O., 2009. High-Mg carbonatitic microinclusions in some Yakutian diamonds – a new type of diamond-forming fluid. Lithos 112, 648–659.

Kogarko, L.N., Henderson, C.M.B., Pacheco, H., 1995. Primary Ca-rich carbonatite magma and carbonate-silicate-sulfide liquid immiscibility in the upper-mantle. Contrib. Mineral. Petrol. 121, 267–274.

Korsakov, A.V., Hermann, J., 2006. Silicate and carbonate melt inclusions associated with diamonds in deeply subducted carbonate rocks. Earth Planet. Sci. Lett. 241, 104–118.

Korsakov, A.V., De Gussem, K., Zhukov, V.P., Perraki, M., Vandenabeele, P., Golovin, A.V., 2009. Aragonite-calcite-dolomite relationships in UHPM polycrystalline carbonate inclusions from the Kokchetav Massif, northern Kazakhstan. Eur. J. Mineral. 21, 1301–1311.

Korsakov, A.V., Golovin, A.V., Sharygin, I.S., 2014. Raman spectroscopic study of mica from ultra-fresh Udachnay-East kimberlites. Proc. GeoRaman XI, St Louis, USA, pp. 141.

Leost, I., Stachel, T., Brey, G.P., Harris, J.W., Ryabchikov, I.D., 2003. Diamond formation and source carbonation: mineral associations in diamonds from Namibia. Contrib. Mineral. Petrol. 145, 15–24.

Litasov, K.D., Shatskiy, A., Ohtani, E., Yaxley, G.M., 2013. Solidus of alkaline carbonatite in the deep mantle. Geology 41, 79–82.

Logvinova, A.M., Wirth, R., Fedorova, E.N., Sobolev, N.V., 2008. Nanometre-sized mineral and fluid inclusions in cloudy Siberian diamonds: new insights on diamond formation. Eur. J. Mineral. 20, 317–331.

Longerich, H.P., Jackson, S.E., Gunther, D., 1996. Laser ablation inductively coupled plasma mass spectrometric transient signal data acquisition and analyte concentration calculation: J. Anal. Atom. Spectrom. 11, 899–604.

Maas, R., Kamenetsky, M.B., Sobolev, A.V., Kamenetsky, V.S., Sobolev, N.V., 2005. Sr, Nd, and Pb isotope evidence for a mantle origin of alkali chlorides and carbonates in the Udachnaya kimberlite, Siberia. Geology 33, 549–552.

MacGregor, I.D., 1974. The system MgO-Al_2O_3-SiO_2: solubility of Al_2O_3 in enstatite for spinel and garnet peridotite compositions. Am. Mineral. 59, 110–119.

Marshintsev, V.K., Migalkin, K.N., Nikolaev, N.C., Barashkov, Y.P., 1976. Unaltered kimberlite of the Udachnaya East pipe. Doklady USSR Acad. Sci. 231, 961–964.

McDonough, W.F., Sun, S.S., 1995. The composition of the Earth. Chem. Geol. 120, 223–253.

McKenzie, D., Jackson, J., Priestley, K., 2005. Thermal structure of oceanic and continental lithosphere. Earth Planet. Sci. Lett. 233, 337–349.

Mernagh, T.P., Kamenetsky, V.S., Kamenetsky, M.B., 2011. A Raman microprobe study of melt inclusions in kimberlites from Siberia, Canada, SW Greenland and South Africa. Spectrochim. Acta A Mol. Biomol. Spectrosc. 80A, 82–87.

Mercier, J.-C., 1979. Peridotite xenoliths and the dynamics of kimberlite intrusion. Proc. 2th Int. Kimb. Conf. 2, 197–212.

Mitchell, R.H., 2008. Petrology of hypabyssal kimberlites: relevance to primary magma compositions. J. Volcanol. Geotherm. Res. 174, 1–8.

Moine, B.N., Grégoirec, M., O'Reilly S.Y., Delpech, G., Sheppard S.M.F., Lorand J.P., Renac, C., Giret, A., Cottin, J.Y., 2004. Carbonatite melt in oceanic upper mantle beneath the Kerguelen Archipelago. Lithos 75, 239–252.

Nixon, P.H., 1995. A review of mantle xenoliths and their role in diamond exploration. J. Geodyn. 20, 305–329.

O'Reilly, S.Y., Griffin, W.L., 2010. The continental lithosphere-asthenosphere boundary: Can we sample it? Lithos 120, 1–13.

Pal'yanov, Y.N., Sokol, A.G., Borzdov, Y.M., Khokhryakov, A.F., Sobolev, N.V., 1999. Diamond formation from mantle carbonate fluids. Nature 400, 417–418.

Palyanov, Y.N., Sokol, A.G., 2009. The effect of composition of mantle fluids/melts on diamond formation processes. Lithos 112, 690–700.

Pearson, D.G., Brenker, F.E., Nestola, F., McNeill, J., Nasdala, L., Hutchison, M.T., Matveev, S., Mather, K., Silversmit, G., Schmitz, S., Vekemans B., Vincze L., 2014. Hydrous mantle transition zone indicated by ringwoodite included within diamond. Nature 507, 221–224.

Pokhilenko, N.P., Sobolev, N.V., Kuligin, S.S., Shimizu, N., 1999. Peculiarities of distribution of pyroxenite paragenesis garnets in Yakutian kimberlites and some aspects of the evolution of the Siberian craton lithospheric mantle. 7th International Kimberlite Conference eds Gurney J.J., Gurney J.L., Pascoe M.D., Richardson S.H., 689–698.

Rudnick, R.L., McDonough, W.F., Chappell, B.W., 1993. Carbonatite metasomatism in the northern Tanzanian mantle: petrographic and geochemical characteristics. Earth Planet. Sci. Lett. 114, 463–475.

Russell, J.K., Porritt, L.A., Lavallee, Y., Dingwell, D.B., 2012. Kimberlite ascent by assimilation-fuelled buoyancy. Nature 481, 352–356.

Schiano, P., Clocchiatti, R., 1994. Worldwide occurrence of silica-rich melts in sub-continental and sub-oceanic mantle minerals. Nature 368, 621–624.

Sharygin, V.V., Golovin, A.V., Pokhilenko, N.P., Sobolev, N.V., 2003. Djerfisherite in unaltered kimberlites of the Udachnaya-East pipe, Yakutia. Dokl. Earth Sci. 390, 554–557.

Sharygin, V.V., Golovin, A.V., Pokhilenko, N.P., Kamenetsky, V.S., 2007a. Djerfisherite in the Udachnaya-East pipe kimberlites (Sakha-Yakutia, Russia): paragenesis, composition and origin. Eur. J. Mineral. 19, 51–63.

Sharygin, V.V., Kamenetsky, V.S., Kamenetskaya, M.B., Seretkin, Y.V., Pokhilenko, N.P., 2007b. Rasvumite from the Udachnaya-East pipe: The first finding in kimberlites. Dokl. Earth Sci. 415, 929–934.

Sharygin, I.S., Golovin, A.V., Pokhilenko, N.P., 2011. Djerfisherite in kimberlites of the Kuoikskoe field as an indicator of enrichment of kimberlite melts in chlorine. Dokl. Earth Sci. 436, 301–307.

Sharygin, I.S., Golovin, A.V., Pokhilenko, N.P., 2012. Djerfisherite in xenoliths of sheared peridotite in the Udachnaya-East pipe (Yakutia): origin and relationship with kimberlitic magmatism. Russ. Geol. Geophys. 53, 247–261.

Sharygin, I.S., Litasov K.D., Shatskiy A.F., Golovin A.V., Ohtani E., Pokhilenko N.P., 2015. Melting phase relations of the Udachnaya-East Group-I kimberlite at 3.0-6.5 GPa: experimental evidence for alkali-carbonatite composition of primary kimberlite melts and implications for mantle plumes. Gondwana Res. 28, 1391–1414.

Sharygin, I.S., Litasov, K.D., Shatskiy, A., Safonov, O.G., Golovin, A.V., Ohtani, E., Pokhilenko, N.P., 2017. Experimental constraints on orthopyroxene dissolution in alkali carbonate melts in the lithospheric mantle: Implications for kimberlite melt composition and magma ascent. // Chem. Geol. 455, 44–56.

Shatskiy, A., Gavryushkin, P.N., Sharygin, I.S., Litasov, K.D., Kupriyanov, I.N., Higo, Y., Borzdov, Y.M., Funakoshi, K., Palyanov, Y.N., Ohtani, E., 2013. Melting and subsolidus phase relations in the system Na_2CO_3-$MgCO_3$±H_2O at 6 GPa and the stability of $Na_2Mg(CO_3)_2$ in the upper mantle. Am. Mineral. 98, 2172–2182.

Shatskiy, A., Litasov, K., Palyanov, Y.N., 2015. Phase relations in carbonate systems at pressures and temperatures of lithospheric mantle: review of experimental data. Russ. Geol. Geophys. 56, 113–142.

Shatskiy, A., Litasov, K., Sharygin I., Ohtani E., 2017. Composition of primary kimberlite melt in a garnet lherzolite mantle source: constraints from melting phase relations in anhydrous Udachnaya-East kimberlite with variable CO_2 content at 6.5 GPa. Gondwana Res. 45, 208–227.

Shu, Q., Brey, G.P., 2015. Ancient mantle metasomatism recorded in subcalcic garnet xenocrysts: Temporal links between mantle metasomatism, diamond growth and crustal tectonomagmatism. Earth Planet. Sci. Lett. 418, 27–39.

Sobolev, A.V., Sobolev, N.V., Smith, C.B., Dubessy, J., 1989. Fluid and melt compositions in lamproites and kimberlites based on the study of inclusions in olivine. Proc. 2th Int. Kimb. Conf.: Kimberlite and related rocks. GSA Spec. Publ. 1(14), 220–240.

Sobolev, N.V., Kaminsky, F.V., Griffin, W.L., Yefimova, E.S., Win, T.T., Ryan, C.G., Botkunov, A.I., 1997. Mineral inclusions in diamonds from the Sputnik kimberlite pipe, Yakutia. Lithos 39, 135–157.

Sobolev, N.V., Logvinova, A.M., Efimova, E.S., 2009a. Syngenetic phlogopite inclusions in kimberlite-hosted diamonds: implications for role of volatiles in diamond formation. Russ. Geol. Geophys. 50, 1234–1248.

Sobolev, N.V., Logvinova, A.M., Zedgenizov, D.A., Pokhilenko, N.P., Malygina, E.V., Kuzmin, D.V., Sobolev, A.V., 2009b. Petrogenetic significance of minor elements in olivines from diamonds and peridotite xenoliths from kimberlites of Yakutia. Lithos 112, 701–713.

Stachel, T., Harris, J.W., 2008. The origin of cratonic diamonds - constraints from mineral inclusions. Ore Geol. Rev. 34, 5–32.

Stone, R.S., Luth, R.W., 2016. Orthopyroxene survival in deep carbonatite melts: implications for kimberlites. Contrib. Mineral. Petrol. 171:63.

Tappe, S., Pearson, G.D., Kjarsgaard, B.A., Nowell, G., Dowall, D., 2013. Mantle transition zone input to kimberlite magmatism near a subduction zone: Origin of anomalous Nd–Hf isotope systematics at Lac de Gras, Canada. Earth Planet. Sci. Lett. 371-372, 235–251.

Tappe, S., Romer, R.L., Stracke, A., Steenfelt, A., Smart, K.A., Muehlenbachs, K., Torsvik, T.H., 2017. Sources and mobility of carbonate melts beneath cratons, with implications for deep carbon cycling, metasomatism and rift initiation. Earth Planet. Sci. Lett. 466, 152–167.

Thomson, A.R., Walter, M.J., Kohn, S.C., Brooker, R.A., 2016. Slab melting as a barrier to deep carbon subduction. Nature 529, 76–79.

Tomilenko, A.A., Kuzmin D.V., Bul'bak T.A., Sobolev N.V., 2017. Primary melt and fluid inclusions in regenerated crystals and phenocrysts of olivine from kimberlites of the Udachnaya-East pipe, Yakutia: the problem of the kimberlite melt. Dokl. Earth Sci. 475, 949–952.

Torsvik, T.H., Burke, K., Steinberger, B., Webb, S.J., Ashwal, L.D., 2010. Diamonds sampled by plumes from the core-mantle boundary. Nature 466, 352–355.

van Achterbergh, E., Griffin W.L., Ryan C.G., Suzanne Y. O'Reilly S.Y.,Pearson N.J., Kivi K., Doyle B.J., 2002. Subduction signature for quenched carbonatites from the deep lithosphere. Geology 30, 743–746.

Veksler, I.V., Nielsen, T.F.D., Sokolov, S.V., 1998. Mineralogy of crystallized melt inclusions from Gardiner and Kovdor ultramafic alkaline complexes: Implications for carbonatite genesis. J. Petrol. 39, 2015–2031.

Veksler, I.V., Lentz, D., 2006. Parental magmas of plutonic carbonatites, carbonate-silicate immisibility and decarbonation reactions: Evidence from melt and fluid inclusions. Pp. 123–150 in: Melt Inclusions in Plutonic Rocks. Volume 36: Quebec, Mineralogical Association of Canada.

Wallace, M.E., Green, D.H., 1988. An experimental determination of primary carbonatite magma composition. Nature 335, 343–346.

Wyllie, P.J., Huang, W.L., 1975. Peridotite, kimberlite, and carbonatite explained in the system CaO-MgO-SiO2-CO2. Geology 3, 621–624.

Yaxley, G.M., Green, D.H., Kamenetsky, V., 1998. Carbonatite metasomatism in the southeastern Australian lithosphere. J. Petrol. 39, 1917–1930.

Yaxley, G.M., Berry, A.J., Kamenetsky, V.S.,Woodland, A.B., Golovin, A.V., 2012. An oxygen fugacity profile through the Siberian Craton — Fe K-edge XANES determinations of $Fe^{3+}/\Sigma Fe$ in garnets in peridotite xenoliths from the Udachnaya East kimberlite. Lithos 140, 142–151.

Zaitsev, A.N., Keller, J., Spratt, J., Jeffries, T.E., Sharigin, V.V., 2009. Chemical composition of nyerereite and gregoryite from natrocarbonatites of Oldoinyo Lengai volcano, Tanzania. Geol. Ore Deposits 51, 608–616.

Zedgenizov, D.A., Rege, S., Griffin, W.L., Kagi, H., Shatsky, V.S., 2007. Composition of trapped fluids in cuboid fibrous diamonds from the Udachnaya kimberlite: LAM-ICPMS analysis. Chem. Geol. 240, 151–162.

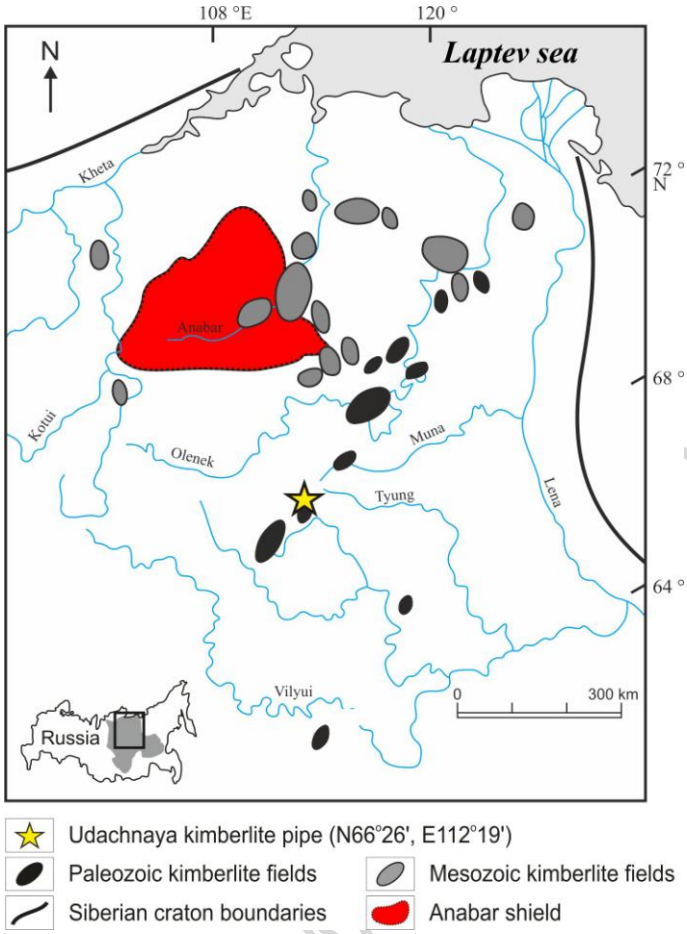

Figure 1. (Colour only online) Location map for the Udachnaya kimberlite pipe after Kinny et al. (1997), Pokhilenko et al. (1999), Sharygin et al. (2011) and references therein. The grey area in the Russia map inset shows the Siberian craton.

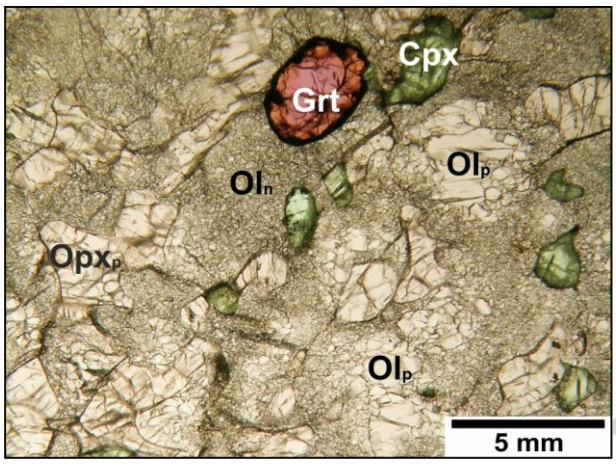

Figure 2. (Colour only online) Transmitted-light optical image of Udachnaya sheared peridotite (sample No. UV-3/05) with mosaic-porphyroclastic texture. Grt–garnet, Cpx–clinopyroxene, Opx–orthopyroxene, Ol_p and Ol_n – porphyroclastic and neoblastic olivine, respectively.

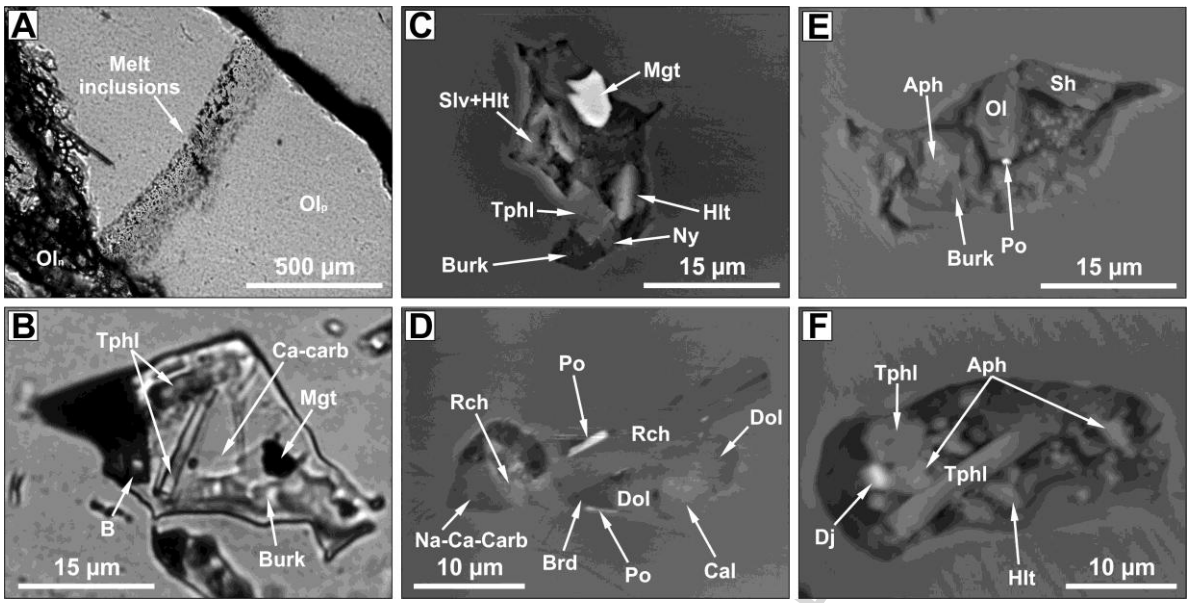

Figure 3. Secondary melt inclusions in olivine from sheared peridotites. (A) Secondary melt inclusions along healed fractures in olivine porphyroclast from Udachnaya sheared peridotite. (B) Transmitted-light optical image of individual crystallized melt inclusion. The behaviour of this inclusion during experimental heating is illustrated in Fig. 7. (C–F) Back-scattered electron images illustrating daughter phase mineralogy of exposed melt inclusions in olivine. EDS spectra of phases in the images and their X-ray maps are presented in Suppl. Fig. 1. Ol_p – porphyroclastic olivine, Ol_n – neoblastic olivine, Ol – daughter olivine, Tphl–tetraferriphlogopite, Rch–richterite, Mgt–magnetite, Hlt–halite, Slv–sylvite, Burk–burkeite, Aph–aphthitalite, Sh–shortite, Ny–nyerereite, Na-Ca carb–Na-Ca-carbonate $Na_2Ca(CO_3)_2$, Cal–calcite, Dol–dolomite, Brd–bradleyite, Po–pyrrhotite, Dj–djerfisherite, B–bubble.

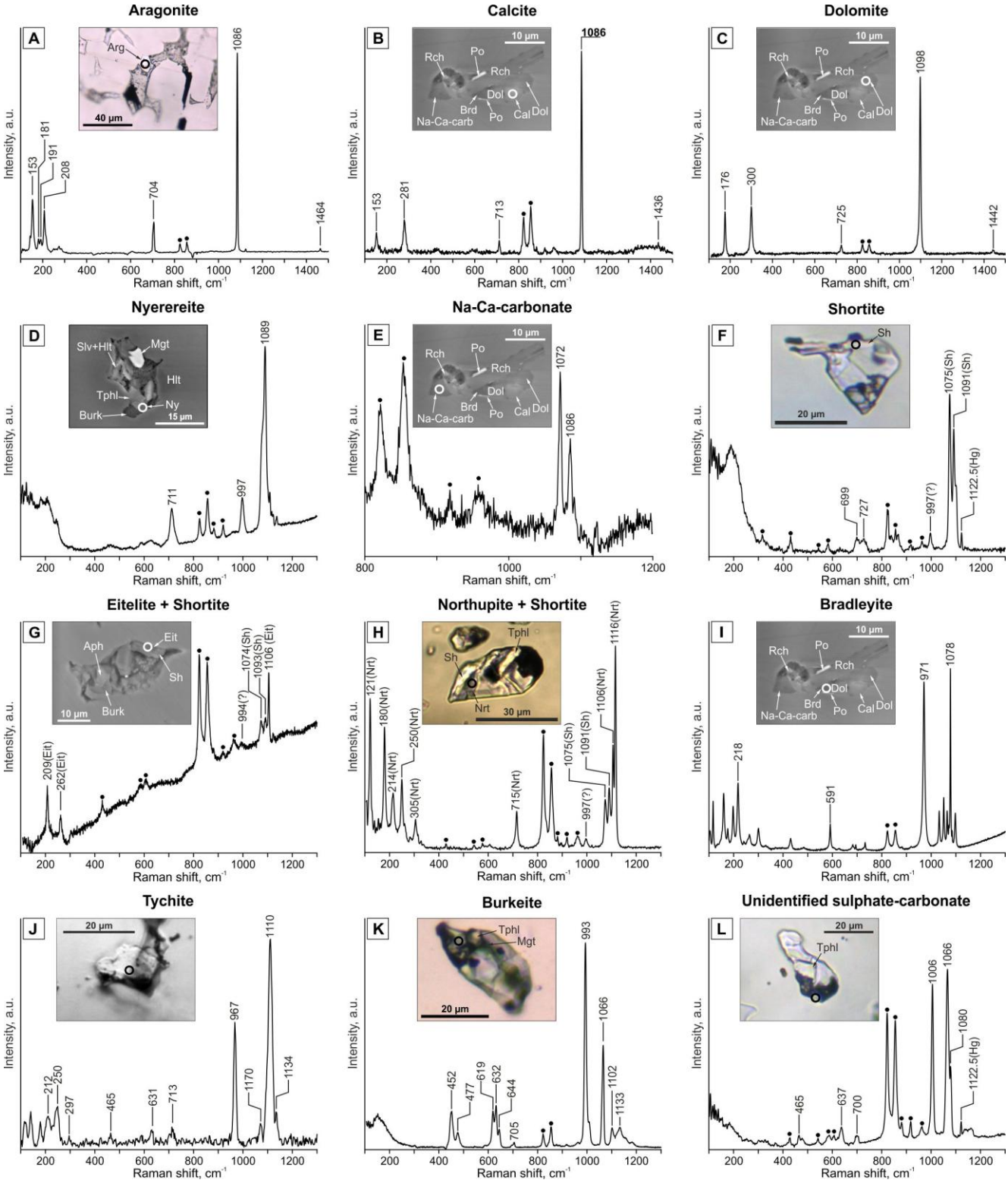

Figure 4. (Colour only online) Raman spectra of carbonates and carbonates with additional anions within melt inclusions in olivine from sheared peridotites of the Udachnaya-East pipe. (A, F, H, J–L) Unexposed inclusions. (B–E, G, I) Exposed inclusions. Circles in images indicate from where Raman spectra were collected. Black circles in Raman spectra are main bands of host olivine. Eit–eitelite, Sh–shortite, Nrt–northupite. The band at 1122.5 cm^{-1} (Hg) in the spectra is a mode of mercury from a luminous tube lamp, which can be used for calibration.

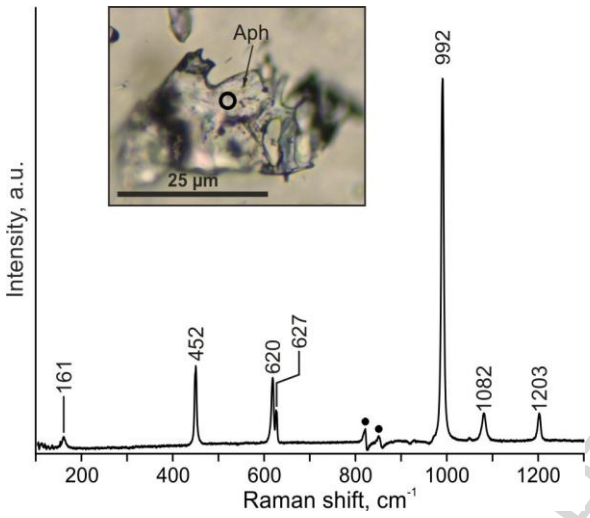

Figure 5. (Colour only online) Raman spectrum of aphthitalite in unexposed inclusions in olivine from sheared peridotites of the Udachnaya-East pipe. The circle in the image indicates from where the Raman spectrum was collected. The black circles in the Raman spectra are the main bands of host olivine.

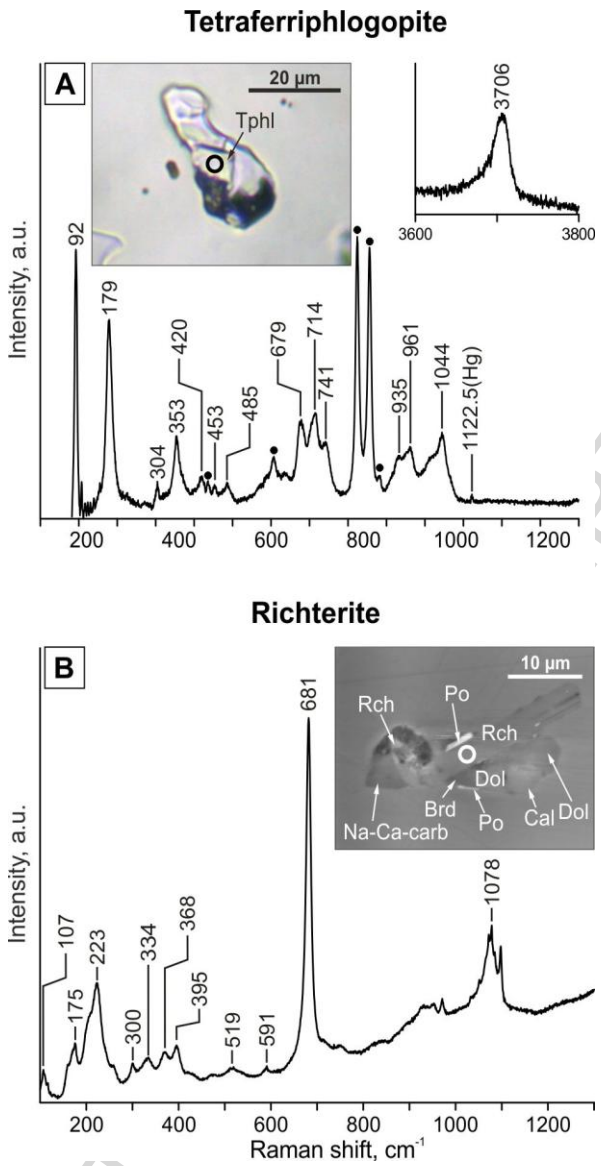

Figure 6. (Colour only online) Raman spectrum of tetraferriphlogopite in unexposed inclusion (A) and richterite in exposed inclusion (B) in olivine from sheared peridotite of the Udachnaya-East pipe. Circles in the images indicate from where Raman spectra were collected. Black circles in the Raman spectra are the main bands of host olivine.

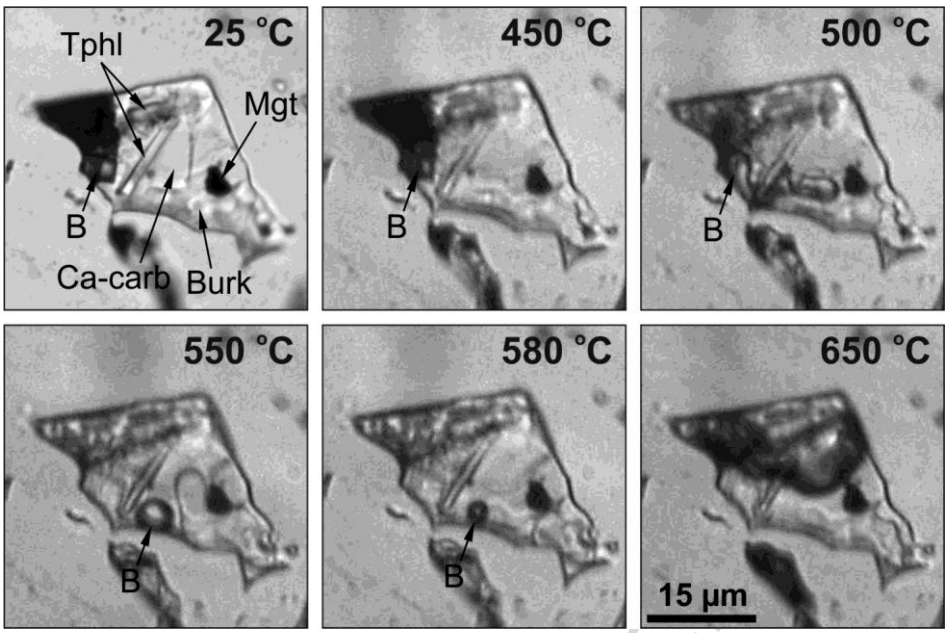

Figure 7. Snapshots in plain transmitted light showing behaviour of a typical secondary melt inclusion in olivine of sheared peridotite during experimental heating: 25 °C–the inclusions before heating; 450 °C–no transformation inside the inclusions; 500 °C – beginning of melting; 550–580 °C – changes in volume ratios of solid phases, melt and bubble (B) within the inclusion; 650 °C – decrepitation of the inclusions.

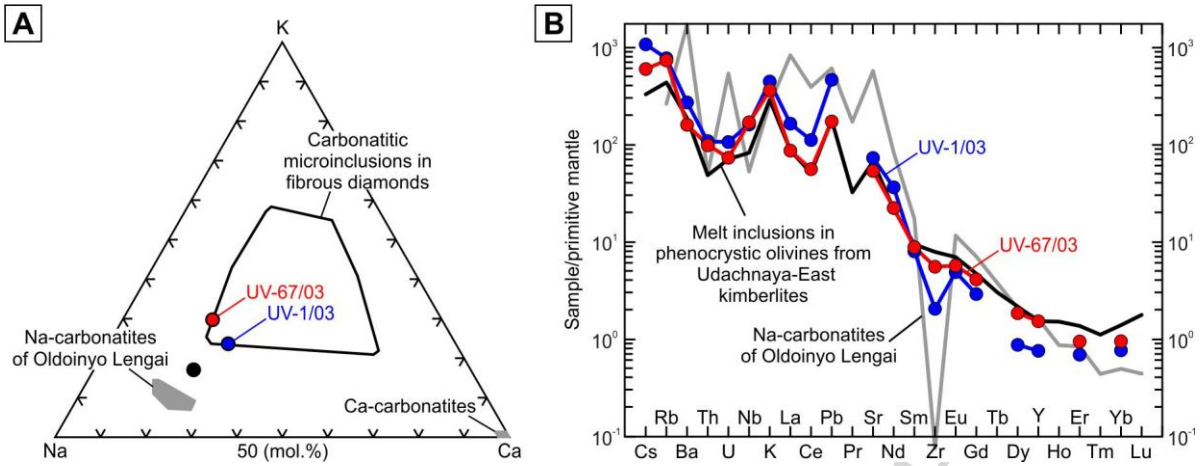

Figure 8. (Colour only online) (A) The average bulk composition of melt inclusions in olivine of Udachnaya-East sheared peridotites (red and blue circles) in comparison with that of melt inclusions in phenocrystic olivines from host kimberlites (black circle) (Kamenetsky et al., 2009a). Compositional ranges of carbonatitic microinclusions in the fibrous diamonds from kimberlites worldwide (Klein-BenDavid et al., 2007, 2009; Zedgenizov et al., 2007), Na-carbonatites of Oldoinyo Lengai and Ca-carbonatites worldwide (Keller and Zaitsev, 2012 and references therein) are contoured. (B) Trace-element composition of melt inclusions in olivine from the sheared peridotites (red and blue circles) and phenocrystic olivines from the host kimberlites (black line) (Kamenetsky et al., 2009a) in comparison with Na-carbonatites of Oldoinyo Lengai (grey line) (Keller and Zaitsev, 2012). Data are normalized to primitive mantle values (McDonough and Sun, 1995).

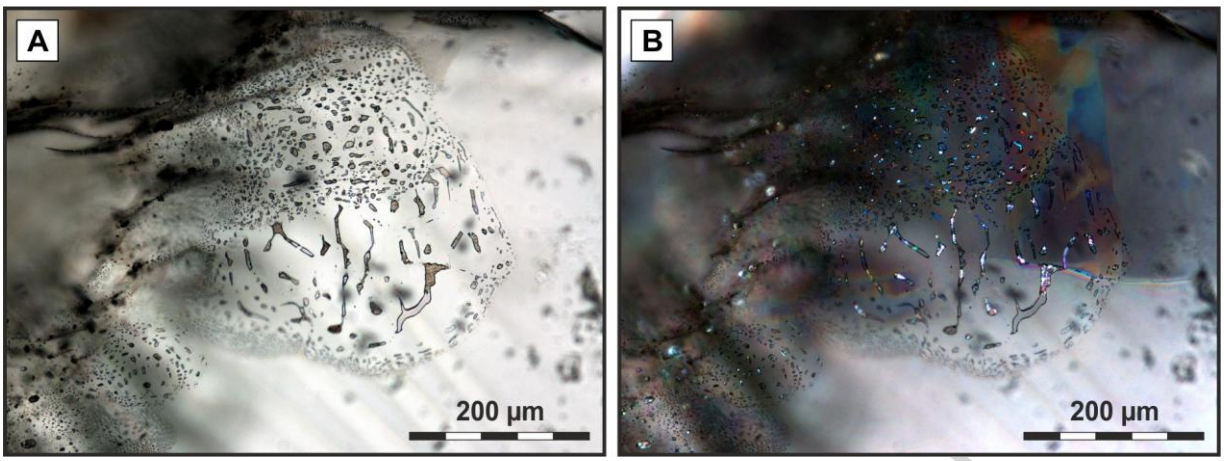

Figure 9. (Colour only online) The secondary melt inclusions along a healed crack within olivine porphyroclast. Plane polarized (a) and cross polarized (b) transmitted light. The very bright phases within the melt inclusions in panel (b) are carbonates.

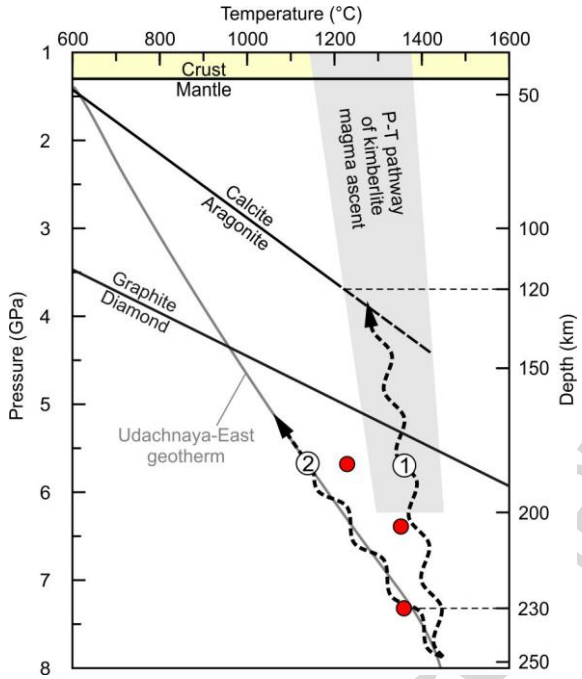

Figure 10. (Colour only online) *T*–*P*-depth scheme displaying the two possible models of infiltration of alkaline carbonatite melt into Udachnaya-East sheared peridotites shown by dashed curves: (1) infiltration during kimberlite magma ascent and (2) *in situ* percolation (see text for explanation). The calcite–aragonite transition is from Irving and Wyllie (1975). Red circles are *T*–*P*-depth estimates of the sheared peridotites. The Udachnaya geotherm is from McKenzie et al. (2005). The grey field shows thermodynamically modelled temperature–depth profiles from 200 km of depth of adiabatically ascending kimberlite magma (Kavanagh and Sparks, 2009). Pressures were converted to depths using the PREM model (Dziewonski and Anderson, 1981).

Table 1. Key petrographic features and T-P-depth estimates of the studied sheared peridotite xenoliths from Udachnaya-East kimberlite pipe.

Sample no.	UV-1/03	UV-67/03	UV-3/05
Rock type/name	Harzburgite	Lherzolite	Lherzolite
Texture*	Porphyroclastic	Mosaic-porphyroclastic	Mosaic-porphyroclastic
Ol	+	+	+
Opx	+	+	+
Cpx	-	+	+
Grt	+	+	+
Mg# in Ol	91.5	90.7	87.5
Mg# in Opx	93.0	92.0	89.1
Ca# in Cpx	-	37.1	35.5
Cr_2O_3 in Grt	11.1	2.8	5.9
CaO in Grt	6.6	4.3	5.8
T, ^oC, FB96	-	1309	1336
P, kbar, MG74	-	66.7	68.7
T, ^oC, T_{BKN}	1229**	1359	1352
P, kbar, P_{BKN}	56.8	73.2	63.9
Depth, km†	179	227	200

* based on classification in (Boullier and Nicolas, 1975; Harte, 1977);
\+ indicates presence of phase: Ol - olivine, Opx - orthopyroxene, Cpx - clinopyroxene, Grt - garnet;
Mg# in Ol = 100·Mg/(Mg+Fe) (at.%) in olivine;
Mg# in Opx = 100·Mg/(Mg+Fe) (at.%) in orthopyroxene;
Ca# in Cpx – 100·Ca/(Ca+Mg+Fe) (at.%) in clinopyroxene;
Cr_2O_3 Grt and CaO Grt – Cr_2O_3 and CaO contents (wt%) in garnet;
FB96 and MG74 – combination of thermometer of Finnerty and Boyd (1987) based on Ca-Mg partition in pyroxenes and Al-in-Opx barometer of MacGregor (1974);
P_{BKN} and T_{BKN} – combination of thermometer and barometer from (Brey and Köhler, 1990);
** for this sample pressure and temperature were estimated using combination of P_{BKN} barometer and Ca-in-Opx thermometer (Brey and Köhler, 1990);
† pressures estimated by Ca-in-Opx/P_{BKN} and T_{BKN}/P_{BKN} thermobarometers were converted to depths using PREM model (Dziewonski and Anderson, 1981).

Table 2. Electron microprobe data for rock-forming (primary) minerals from sheared Udachnaya-East peridotites

Sample No	UV-1/03			UV-67/03				UV-3/05			
Mineral	Ol	Opx	Gt	Ol	Opx	Cpx	Gt	Ol	Opx	Cpx	Gt
SiO_2	41.19(28)	57.47(20)	40.88(21)	40.57(14)	57.79(4)	55.52(9)	42.52(11)	39.86(12)	56.62(31)	55.29(6)	41.62(17)
TiO_2	n.a.	0.01(1)	0.06(1)	n.a.	0.08(1)	0.16(1)	0.43(2)	n.a.	0.18(2)	0.33(1)	0.15(3)
Al_2O_3	n.a.	0.47(2)	14.05(22)	n.a.	0.68(1)	1.92(1)	20.49(2)	n.a.	0.67(1)	1.76(2)	17.93(13)
Cr_2O_3	0.06(1)	0.33(2)	11.07(25)	0.02(1)	0.21(2)	0.91(2)	2.82(10)	0.02(1)	0.19(1)	0.78(1)	5.94(15)
FeO*	8.26(8)	4.79(10)	6.92(5)	8.97(5)	5.34(2)	3.37(1)	7.38(2)	12.06(7)	7.14(4)	4.68(7)	7.96(5)
MnO	0.11(1)	0.13(2)	0.35(2)	0.10(1)	0.13(1)	0.12(1)	0.30(2)	0.12(1)	0.15(1)	0.13(1)	0.32(4)
MgO	50.21(15)	35.67(73)	19.43(17)	49.14(30)	34.47(17)	19.00(7)	21.64(12)	47.28(15)	32.87(15)	18.88(5)	19.67(15)
CaO	0.05(1)	0.88(1)	6.63(7)	0.05(1)	0.91(2)	17.16(4)	4.30(8)	0.05(1)	0.97(3)	16.45(3)	5.76(6)
Na_2O	n.a.	0.04(2)	0.02(1)		0.26(7)	1.71(6)	0.07(1)	n.a.	0.24(2)	1.66(2)	0.03(1)
K_2O	n.a.	n.a.	n.a.		n.a.	0.04(1)	n.a.	n.a.	n.a.	0.04(1)	n.a.
NiO	0.39(1)	n.a.	n.a.	0.35(1)	n.a.	n.a.	n.a.	0.31(2)	n.a.	n.a.	n.a.
Total	100.27	99.78	99.42	99.19	99.85	99.91	99.94	99.70	99.03	99.99	99.38

Formula based on oxygen number

Sample No	UV-1/03			UV-67/03				UV-3/05			
Mineral	Ol	Opx	Gt	Ol	Opx	Cpx	Gt	Ol	Opx	Cpx	Gt
Oxygen	4	6	12	4	6	6	12	4	6	6	12
apfu											
Si	1.001	1.977	3.028	1.000	1.989	1.994	3.026	0.992	1.983	1.992	3.033
Ti	0.000	0.000	0.004	0.000	0.002	0.004	0.023	0.000	0.005	0.009	0.008
Al	0.000	0.019	1.227	0.000	0.027	0.081	1.719	0.000	0.028	0.075	1.540
Cr	0.001	0.009	0.648	0.000	0.006	0.026	0.159	0.000	0.005	0.022	0.342
Fe	0.168	0.138	0.428	0.185	0.154	0.101	0.439	0.251	0.209	0.141	0.485
Mn	0.002	0.004	0.022	0.002	0.004	0.004	0.018	0.003	0.004	0.004	0.020
Mg	1.818	1.829	2.146	1.805	1.768	1.017	2.295	1.754	1.716	1.014	2.137
Ca	0.001	0.032	0.527	0.001	0.033	0.661	0.328	0.001	0.036	0.635	0.450
Na	0.000	0.003	0.004	0.000	0.017	0.119	0.010	0.000	0.016	0.116	0.004
K	0.000	0.000	0.000	0.000	0.000	0.002	0.000	0.000	0.000	0.002	0.000
Ni	0.008	0.000	0.000	0.007	0.000	0.000	0.000	0.006	0.000	0.000	0.000
Total	2.999	4.010	8.033	3.000	4.001	4.009	8.017	3.008	4.004	4.010	8.019

cations			

Numbers in parentheses are one standard deviation in terms of the last significant digits, determined by multiply analyses of the individual mineral. At least 3 analyses were performed for each mineral in each xenolith. * all Fe as FeO. n.a. – not analyzed. Apfu – atom per formula unit.

Table 3. Normalized* bulk chemical compositions of secondary melt inclusions in olivine from Udachnaya-East sheared peridotites (by laser-ablation inductively-coupled-plasma mass-spectrometry)

Sample No	ppm B	wt% Na_2O	ppm Cl	wt% K_2O	wt% CaO	ppm Rb	ppm Sr	ppm Y	ppm Zr	ppm Nb	ppm Cs	ppm Ba	ppm La	ppm Ce	ppm Nd	ppm Sm	ppm Eu	ppm Gd	ppm Dy	ppm Er	ppm Yb	ppm Pb	ppm Th	ppm U
UV-67/03	1601	16.1	72030	14.5	11.5	525	1596	3.4	23	119	26	2002	118	206	49	3.5	0.8	1.7	0.6	0.3	0.4	78	9.5	2.4
UV-01/03	2442	16.2	61333	11.7	15.5	499	1165	6.9	62	122	14	1172	62	103	30	3.8	0.9	2.4	1.3	0.4	0.4	29	8.7	1.6

* As the internal standard concentrations in the analyzed melt inclusions could not be independently quantified all the data represent relative values or element ratios that are sufficient to trace principal geochemical characteristics (e.g., relative enrichment of alkali elements over Ca or LREE over HREE). The compositions are calculated based on the assumption of 50 wt% total for analyzed elements, the same assumption was previously applied for melt inclusions in kimberlitic olivine by Kamenetsky et al. (2009). This approach facilitates comparison of the current and previous results.

Table 4. Comparison of mineral assemblage of the melt inclusion in olivine of the studied Udachnaya-East sheared peridotites with mineral assemblage of melt inclusions in phenocrystic olivine from host Udachnaya-East kimberlites, groundmass mineralogy of unaltered Udachnaya-East kimberlites, as well as with mineral assemblage of crystallized primary melt inclusions in magnetite phenocrysts of the Catanda carbonatite lavas and olivine of Kovdor carbonatites.

Mineral	Symbol	Formula	Melt inclusion in olivine of Udachnaya-East sheared peridotites (this study)	Melt inclusion in Udachnaya-East phenocrystic olivine (Golovin et al., 2003, 2007; Kamenetsky et al., 2004; Mernagh et al., 2011)	Groundmass of unaltered Udachnaya-East kimberlites (Kamenetsky et al., 2004, 2008, 2009, 2012, 2014; Golovin et al., 2007; Sharygin et al., 2007a, 2007b)	Crystallized melt inclusions in magnetite phenocrysts of the Catanda carbonatite lavas (Campeny et al., 2015)	Crystallized primary melt inclusions in olivine of Kovdor carbonatites (Veksler and Lentz, 2006; Veksler et al., 1998)
Carbonates							
Na-carbonate	Na-Ca-Carb	$Na_2Ca(CO_3)_2$	●				
Nyerereite	Nye	$(Na,K)_2Ca(CO_3)_2$	●	●	●	●	●
Shortite	Sht	$Na_2Ca_2(CO_3)_3$	●	●	●	●	●
Eitelite	Eit	$Na_2Mg(CO_3)_2$	●				●
Dolomite	Dol	$CaMg(CO_3)_2$	●	●		●	●
Aragonite	Arg	$CaCO_3$	●				
Calcite	Cal	$CaCO_3$	●	●	●	●	●
Carbonates with additional anions							
Northupite	Nrt	$Na_3Mg(CO_3)_2Cl$	●	●	●	●	●
Burkeite	Burk	$Na_6(CO_3)(SO_4)_2$	●	●			
Tychite	Tych	$Na_6Mg_2(CO_3)_4(SO_4)$	●				
Bradleyite	Brd	$Na_3Mg(PO_4)(CO_3)$	●				●
Sulphates							
Aphthitalite	Aph	$K_3Na(SO_4)_2$	●	●	●		
Phosphates							
Apatite	Ap	$Ca_5(PO_4)_3(F,Cl,OH)$	●	●	●	●	●
Sulphides							
Pyrrhotite	Po	$Fe_{1-x}S$	●	●	●	●	
Pentlandite	Pn	$(Fe,Ni)_9S_8$	●	●	●		
Djerfisherite	Dj	$K_6(Na,Cu)(Fe,Ni,Cu)_{24}S_{26}Cl$	●	●	●		●
Rasvumite	Rs	KFe_3S_4	●		●	●	
Chlorides							
Halite	Hlt	NaCl	●	●	●	●	
Sylvite	Slv	KCl	●	●	●	●	
Chloromagnesite	Cmgn	$MgCl_2$	●				
Oxides							
Rutile	Ru	TiO_2	●		●		
Perovskite	Prv	$CaTiO_3$	●	●	●	●	
Ilmenite	Ilm	$FeTiO_3$	●	●	●		
Chromite	Chr	$(Fe,Mg)(Cr,Al)_2O_4$	●	●	●		
Ti-Magnetite	Ti-Mgt	$Fe^{2+}(Fe^{3+},Ti)_2O_4$	●	●	●		
Magnetite	Mgt	$FeFe_2O_4$	●	●	●	●	
Silicates							
Tetraferriphlogopite	Tphl	$KMg_3FeSi_3O_{10}(F,Cl,OH)$	●	●			●

Phlogopite	Phl	$KMg_3AlSi_3O_{10}(F,Cl,OH)$	●	●	●	●	
Olivine	Ol	$(Mg,Fe)_2SiO_4$	●	●	●	●	●
Diopside	Di	$CaMgSi_2O_6$	●	●	●	●	●
Sodalite	Sdl	$Na_8Al_6Si_6O_{24}Cl_2$	●	●	●	●	●
Richterite	Rch	$Na_2Ca(Mg,Fe)_5Si_8O_{22}(OH)_2$	●				